Charting circumstellar chemistry of carbon-rich asymptotic giant branch stars: III. SiO and SiS abundances

A&A, 709, A216 (2026)
https://doi.org/10.1051/0004-6361/202558602

Astronomy & Astrophysics

Charting circumstellar chemistry of carbon-rich asymptotic giant branch stars

III. SiO and SiS abundances

R. Unnikrishnan[1,⋆], E. De Beck[1], L.-Å. Nyman[1,2,3], H. Olofsson[1], W. H. T. Vlemmings[1], M. Maercker[1], M. Van de Sande[4], T. J. Millar[5], T. Danilovich[6,7], M. Andriantsaralaza[1], S. B. Charnley[8], and M. G. Rawlings[9]

[1] Department of Space, Earth and Environment, Chalmers University of Technology, 412 96 Gothenburg, Sweden
[2] Joint ALMA Observatory (JAO), Alonso de Córdova 3107, Vitacura 763-0355, Casilla 19001, Santiago, Chile
[3] European Southern Observatory (ESO), Alonso de Córdova 3107, Vitacura 763-0355, Santiago, Chile
[4] Leiden Observatory, Leiden University, PO Box 9513, 2300 RA Leiden, The Netherlands
[5] Astrophysics Research Centre, School of Mathematics and Physics, Queen's University Belfast, University Road, Belfast BT7 1NN, UK
[6] School of Physics & Astronomy, Monash University, Wellington Road, Clayton 3800, Victoria, Australia
[7] Institute of Astronomy, KU Leuven, Celestijnenlaan 200D, 3001 Leuven, Belgium
[8] NASA Goddard Space Flight Center, 8800 Greenbelt Road, Greenbelt, MD 20771, USA
[9] Gemini Observatory / NSF NOIRLab, 670 N. A'ohoku Place, Hilo, HI 96720, USA

Received 16 December 2025 / Accepted 6 April 2026

ABSTRACT

Context. The circumstellar envelopes of AGB stars are sites of rich molecular chemistry. The present understanding of C-rich AGB chemistry largely relies on observations of the archetypal carbon star IRC+10 216. Current molecular abundance estimates for carbon stars are based either on single-dish spectra sampling a range of excitation conditions, or on interferometric mapping of a few lines.
Aims. We aim to estimate the circumstellar abundances of SiO, SiS, and their most abundant isotopologues (^{29}SiO, ^{30}SiO, ^{29}SiS, ^{30}SiS, and Si^{34}S) for a sample of five carbon stars. This study compares molecular abundances across the sources, tests chemical modelling predictions, and examines whether IRC+10 216 is representative of the broader carbon star population.
Methods. We derived molecular abundances using detailed 1D non-local thermodynamic equilibrium (non-LTE) radiative transfer (RT) modelling, constrained by both morphological and excitation information obtained from spatially resolved ALMA maps and single-dish observations. We further compared the derived abundances to chemical modelling results.
Results. We obtain good fits to the SiO and SiS line profiles, and derived well-constrained abundance profiles and reliable isotopic ratios for all sources except AFGL 3068. While the SiS peak abundances are very similar across the sample ($2.0 \times 10^{-6} - 4.7 \times 10^{-6}$), we find that the SiO peak abundances of the rest of the stars are a factor of ∼5 larger than that of IRC +10 216. The e-folding radii (R_e) are in the range $1.3 \times 10^{16} - 7.0{\times}10^{16}$ cm for SiO and $6.0 \times 10^{15} - 1.0{\times}10^{17}$ cm for SiS. The R_e increases with gas density for both SiO and SiS. Our RT models cannot simultaneously fit the low- and high-J SiO lines of IRC+10216. Chemical models reproduce the derived SiO abundance profiles well, while over-predicting the SiS R_e values.
Conclusions. Our models highlight the necessity of having spatially resolved observations across a broad range of excitation conditions to robustly constrain molecular abundance profiles, while also making evident the limitations inherent in 1D RT modelling using simplified (circum)stellar models. We find that the currently assumed SiS photodissociation rate in chemical models is underestimated.

Key words. astrochemistry – radiative transfer – stars: abundances – stars: AGB and post-AGB – stars: carbon – circumstellar matter

1. Introduction

The circumstellar envelopes (CSEs) of asymptotic giant branch (AGB) stars are rich in gas and dust, and provide ideal conditions for a wide range of astrochemical processes leading to the formation of numerous molecular species (e.g. Cernicharo et al. 2000; Höfner & Olofsson 2018; Unnikrishnan et al. 2024; Agúndez et al. 2020; Van de Sande et al. 2019). In carbon-rich (C-type) AGB CSEs, where the photospheric carbon-to-oxygen ratio (C/O) exceeds unity, complex molecules, including long carbon chains (e.g. Agúndez et al. 2017; Gong et al. 2015; Woods et al. 2003; Unnikrishnan et al. 2024) and possibly also polycyclic aromatic hydrocarbons (PAHs, e.g. Cherchneff 2012; Tielens 2008; Zeichner et al. 2023; Anand et al. 2023) can form efficiently. Molecules as large as C_{60} and C_{70} have been detected in planetary nebulae, which are the descendants of AGB CSEs (Cami et al. 2010). The extended outflows from these stars shape the chemical composition of the interstellar medium (ISM), enriching it with the raw material for future star and planet formation (e.g. Höfner & Olofsson 2018; Tielens 2005; Matsuura et al. 2009; Kobayashi et al. 2011).

Several molecules commonly found in C-type AGB CSEs, such as CO, C_2H_2, CS, SiO, and SiS, originate close to the stellar photosphere and are released into the expanding outflow. These species are often classified as parent molecules (see Woods et al. 2003; Agúndez et al. 2020). In contrast, daughter species such as CN, HNC, and C_4H (Agúndez et al. 2017, 2020) form further out in the envelope, as a result of photodissociation and subsequent

⋆ Corresponding author: ramlal.unnikrishnan@chalmers.se

Table 1. Basic source properties.

Source	$\dot{M}_{H_2}$ [a] ($M_\odot$ yr^{-1})	Distance[b] (pc)	v_{sys} (LSRK, km s^{-1})	v_∞ (LSRK, km s^{-1})	$\dot{M}_{H_2}/v_\infty$ ($M_\odot$ yr^{-1} km^{-1} s)
IRAS 15194−5115	2.2×10^{-5}	696	−15.0	21.5	1.0×10^{-6}
IRAS 15082−4808	2.2×10^{-5}	1050	−3.3	19.5	1.1×10^{-6}
IRAS 07454−7112	8.3×10^{-6}	583	−38.7	13.0	6.4×10^{-7}
AFGL 3068	4.2×10^{-5}	1220	−30.0	14.0	3.0×10^{-6}
IRC +10 216	1.5×10^{-5}	190	−26.5	14.5	1.0×10^{-6}

Notes. $\dot{M}_{H_2}$ is the H_2 mass-loss rate, and v_{sys} and v_∞ denote the systemic and expansion velocities, respectively. The full list of stellar and CSE properties that are inputs to the RT models is given in Paper II (see their Table 3). [a]Paper II; [b]Andriantsaralaza et al. (2022).

chemical reactions. Across the CSE, molecular abundances are modified by the complex interplay of processes such as gas-phase chemistry, dust-gas interactions, and photodissociation (e.g. Van de Sande et al. 2023). High-resolution observations and detailed modelling are required to trace the changing physical and chemical structure of these CSEs.

This work is the third in a series of papers that utilise the high angular resolution and sensitivity of the Atacama Large Millimeter/submillimeter Array (ALMA), to investigate the molecular chemistry in C-type AGB CSEs, extending beyond the well-studied, nearby carbon star IRC+10 216 (see e.g. Agúndez et al. 2012, 2017; Cernicharo et al. 2000; Pardo et al. 2022; Siebert et al. 2022; Velilla Prieto et al. 2015; Tuo et al. 2024, and references therein), to observationally evaluate its often attributed status as an archetypal carbon star. Unnikrishnan et al. (2024, hereafter Paper I) present spatially resolved, unbiased ALMA spectral surveys of three carbon stars, revealing similar chemical diversity and morphological complexity as IRC+10 216 (Velilla-Prieto et al. 2019; Agúndez et al. 2017; Patel et al. 2011; Cernicharo et al. 2000). Unnikrishnan et al. (2025, hereafter Paper II) investigated the circumstellar dust and gas properties of five carbon stars, including IRC+10 216 itself, using radiative transfer (RT) modelling of both dust and CO line emission. They also retrieved robust circumstellar radial abundance profiles of CS through non-local thermodynamic equilibrium (non-LTE) RT modelling, constrained by the ALMA data from Paper I and complementary single-dish (SD) observations.

Unlike CS, which can easily be formed under thermodynamical equilibrium in C-rich envelopes due to the presence of large amounts of carbon (e.g. Agúndez et al. 2020; Danilovich et al. 2018), the formation of silicon-bearing refractory species such as SiO and SiS may depend on several factors, including freeze-out onto the dust and the possible need for shock chemistry (e.g. Cherchneff 2012) to form them in large amounts. Both SD studies (e.g. Woods et al. 2003; Schöier et al. 2007; Agúndez et al. 2012; Van de Sande et al. 2018a; Danilovich et al. 2018; Massalkhi et al. 2019, 2024) and standalone modelling of interferometric data (e.g. Schöier et al. 2006; Agúndez et al. 2017; Velilla-Prieto et al. 2019) have been used to constrain the circumstellar abundances of parent species such as CS, SiO, and SiS. Though a few studies combining both SD and interferometric observations have been done for S- and M-type stars (e.g. Brunner et al. 2018; Danilovich et al. 2019), to our knowledge, Paper II presents the first such models of C-type CSEs. Such integrated modelling, simultaneously employing both excitation and morphological constraints, represents a necessary advancement in accurately determining molecular abundances in CSEs. For this study, we modelled the species SiO and SiS, both of which are characterised by centrally peaked brightness distributions, using the same approach that was employed to model the CS emission in Paper II (see Sect. 3).

2. Source sample and observations

2.1. The sources

Our carbon star sample is the same as in Paper II, consisting of five high mass-loss rate (MLR), late-AGB phase sources, IRAS 15194−5115 (II Lup), IRAS 15082−4808 (V358 Lup), IRAS 07454−7112 (AI Vol), AFGL 3068 (LL Peg), and IRC +10 216 (CW Leo). The basic details of the sources are listed in Table 1. The physical properties of the sources, derived using dust and CO RT modelling, have been presented in Paper II.

2.2. Spectral line surveys

Multi-aperture spectra were extracted from our ALMA band 3 (85–116 GHz) spectral survey cubes of SiO, SiS, and their major isotopologues (^{29}SiO, ^{30}SiO, ^{29}SiS, ^{30}SiS and Si^{34}S), following the same procedure as in Paper II. The line cubes were convolved to progressively larger circular Gaussian beams, with full width at half maximum (FWHM) beginning at the major-axis size of the original synthesised beam and gradually increasing until the resulting line flux reached a plateau, implying that all detected emission has been recovered. Extracting spectra from these convolved cubes allows tracing the line fluxes across different spatial scales and map the radial variations in line intensities. The spectral line profiles extracted from these cubes represent those that would result from observations using an SD telescope with the corresponding Gaussian beam size. The beam sizes listed along with the ALMA spectra in Figs. 2, 4, and B.1–B.30 denote the FWHMs of the circular Gaussian beams of the cubes from which the corresponding spectra were extracted. Comparing with archival SD observations (Woods et al. 2003), we find no evidence of resolved out flux in the lines of these species in our ALMA observations. We complement these data with SD SiO and SiS lines from our APEX surveys. For IRAS 15194−5115, we also use lines from our *Herschel*/HIFI survey. For all details of our ALMA, APEX, and HIFI observations, we refer the reader to Paper I and Paper II. The lines used in this work are listed in Tables A.1–A.7.

2.3. Supplementary observations

We used SiO and SiS lines obtained from the literature as additional constraints to our RT models (Tables A.1–A.7). For IRAS 07454−7112 and AFGL 3068, we used Atacama Compact Array (ACA) observations of SiO J = 5–4, SiS

J = 12–11, ^{29}SiS J = 13–12, and ^{30}SiS J = 19–18, from the DEATHSTAR project (Ramstedt et al. 2020; Andriantsaralaza et al. 2021). The ^{29}SiO J = 8–7 line was also obtained towards IRAS 07454−7112 from the ACA data, but was not detected for AFGL 3068. The synthesised beam size of the ACA observations was comparable to the size of the molecular emitting regions, meaning that all emission is recovered, but we could not extract any information about the radial emission distribution using multi-aperture spectra as we do with the ALMA 12 m array data. Hence, for use in constraining RT models, we treat these lines as if they were single-dish observations.

For IRAS 15194−5115 and IRAS 07454−7112, we compared our APEX SiS line spectra to those from Danilovich et al. (2018), and found them to be identical within the calibration uncertainties. For IRAS 07454−7112, we include in this work the APEX SiS J = 16–15 and 19–18 lines from Danilovich et al. (2018) which were not covered in our APEX survey.

For IRC+10216, we use interferometric line cubes that combined ALMA observations with IRAM 30 m on-the-fly (OTF) maps, for the J = 2–1 lines of SiO, ^{29}SiO, and ^{30}SiO, and the J = 5–4 and 6–5 lines of SiS, ^{29}SiS, ^{30}SiS, and Si^{34}S, from Velilla-Prieto et al. (2019). As this nearby (∼190 pc, see Table 1) source is very extended on the sky, the OTF observations help recover all the emission even at the most extended scales, that would be resolved out in the standalone ALMA observations, which have a maximum recoverable scale (MRS) of ∼23–32″ (Velilla-Prieto et al. 2019). We also obtained a set of SD spectra observed using the IRAM 30 m telescope for both SiO and SiS towards IRC+10216, from Agúndez et al. (2012). These lines included SiO lines from J = 2–1 to 8–7, and SiS lines J = 5–4, 6–5 and J = 8–7 to 19–18. We also used the SiO J = 1–0 and the SiS J = 2–1 lines for IRC+10216, observed using the Yebes 40 m telescope, from Massalkhi et al. (2024). In addition to these, we obtained archival SiS J = 5–4 ALMA observations towards IRC+10216 (project 2015.1.01271.S, PI: D. Keller), which contained a total power map, along with ALMA 12 m and ACA observations. We combined these datasets using the same process as employed in Paper I, and extracted multi-aperture spectra from the combined cube.

3. Radiative transfer modelling

3.1. Molecular data

We take into account both radiative and collisional excitation in our RT modelling of both SiO and SiS. For the radiative part, in our ^{28}SiO, ^{29}SiO, ^{30}SiO models, we include energy levels J = 0–40, from both the v = 0 and v = 1 vibrational levels, leading to a total of 82 levels and 160 radiative transitions. Energies and radiative transition data were sourced from the Jet Propulsion Laboratory (JPL) spectroscopic database[1] (Pickett et al. 1998). The molecular data for ^{28}SiS and its studied isotopologues (^{29}SiS, ^{30}SiS and Si^{34}S) are from the Cologne Database for Molecular Spectroscopy[2] (CDMS, Müller et al. 2005; Endres et al. 2016) catalogue, and are the same as used by Danilovich et al. (2019). For ^{28}SiS, we include energy levels from J = 0 to 99 from each of the vibrational levels v = 0, 1, and 2, amounting to a total of 300 levels and 891 radiative transitions, including ro-vibrational transitions. For the other SiS isotopologues studied in this work, we included energy levels from J = 0 to 40 in the vibrational levels v = 0 and v = 1, totalling 82 levels, with 160 radiative transitions.

For collisional excitation, the v = 0 SiO–H_2 and SiS-H_2 collisional rates, scaled and extrapolated from the SiO–H_2 rates by Dayou & Balança (2006), covering levels up to J = 40 and giving a total of 820 collisional rate coefficients, were used for all studied isotopologues. Our RT code can only take into account one collision partner and hence we have not taken into consideration collisions with other partners, such as He. However, we do not expect this to significantly affect the modelling results, as the number density of He is expected to be only ∼17% of that of H_2 (assuming solar number densities, e.g. Asplund et al. 2009), and given the significant contribution of radiative excitation to the studied lines (see Sect. 5.3).

3.2. Modelling procedure

We adopt a spherically symmetric, smooth CSE model, with an isotropic, constant MLR as in Paper II. The stellar, dust, and gas input parameters for the RT models are taken from the SED fitting and CO modelling results presented in Paper II (see their Table 3). The MLRs (Table 1) used as inputs to the RT code are those of molecular hydrogen, H_2-MLR, and they are derived in Paper II. The circumstellar number densities used in the RT analysis are consequently H_2 densities. To a first approximation, assuming solar mass fractions, the total gas MLR, considering also the contribution of He, can be roughly estimated from the H_2-MLR by multiplying it by a factor of ∼1.4 (the reciprocal of the solar Hydrogen mass fraction). However, we have not made such a correction in this work as the scaling factor falls well within the estimated uncertainties on the derived MLRs (factor of ∼2–3, see Paper II).

We use the latest version of the 1D accelerated lambda iteration (ALI) non-LTE spectral line RT code (Maercker et al. 2008; Danilovich et al. 2018, 2019) to model the line emission in this work. All fractional abundances used in this work are defined as relative abundances with respect to molecular hydrogen (H_2), as in Paper II. We use Gaussian abundance profiles, given by

$$f(r) = f_0 \exp\left(-\left(\frac{r}{R_e}\right)^2\right), \quad (1)$$

with the peak abundance (f_0) and the e-folding radius (R_e) as free parameters in the modelling. To find the best-fit models, we employ χ^2 minimisation between the modelled and observed integrated line intensities, taking into account the spatial constraints from the multi-aperture ALMA spectra, and covering a large range of excitation conditions traced by multiple SD lines. We refer to Paper II for a detailed description of the overall modelling technique and the χ^2 minimisation methods adopted. In this work, we model all the above isotopologues with both f_0 and R_e as free parameters, and use the intersection of the respective 1σ χ^2 contours of all modelled isotopologues per molecule, to determine the overall range of plausible models for each species.

The $f_0 - R_e$ grids used for the five sources can be found in Figs. 1, 3, and 5. The grids were chosen to encompass the expected ranges of SiO and SiS abundances and radial extents in carbon stars from previous SD estimates (e.g. Woods et al. 2003; Agúndez et al. 2012; Danilovich et al. 2018; Massalkhi et al. 2019, 2024) and chemical modelling studies (e.g. Maes et al. 2023; Van de Sande et al. 2025). We note that though the upper limits of the R_e space sampled sometimes become comparable to the corresponding CO photodissociation radii, the determined best-fit values of R_e for all sources fall well within

[1] https://spec.jpl.nasa.gov
[2] https://cdms.astro.uni-koeln.de

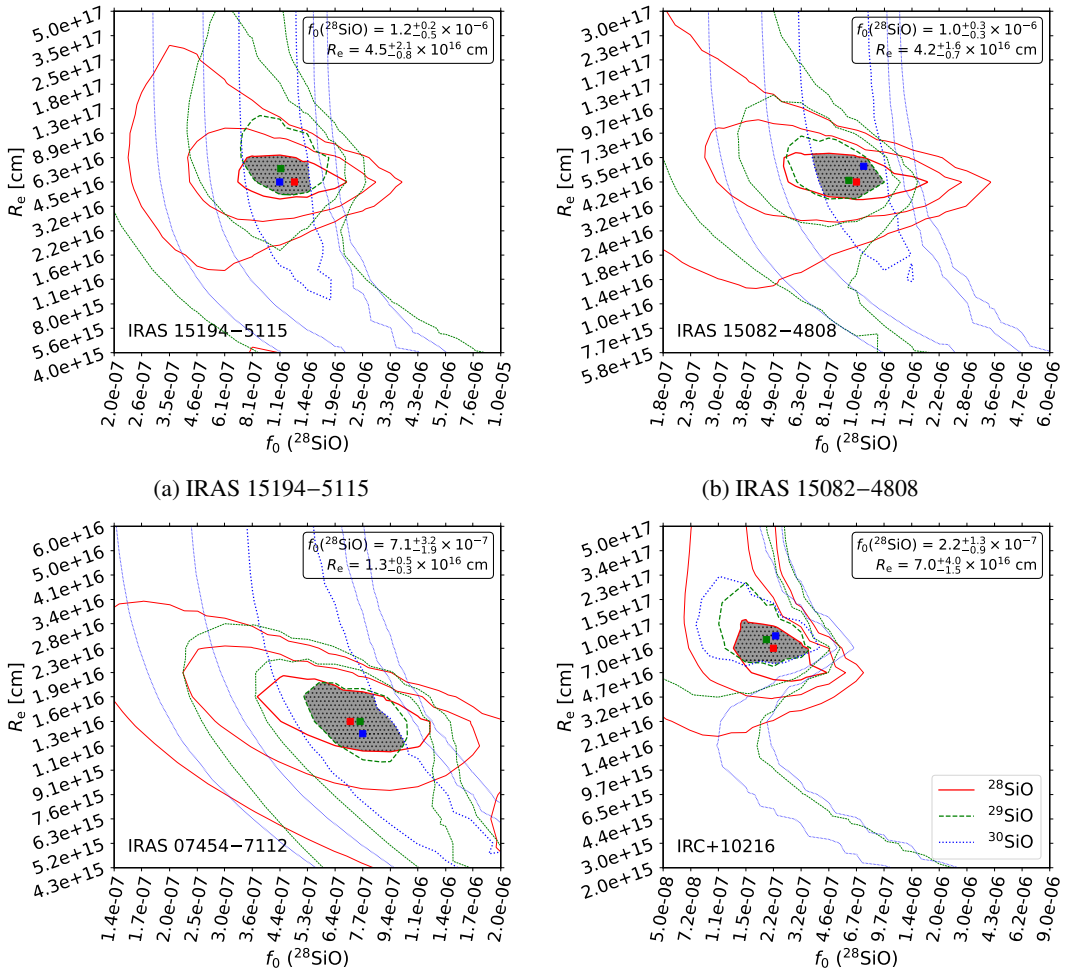

(a) IRAS 15194−5115 (b) IRAS 15082−4808

(c) IRAS 07454−7112 (d) IRC +10 216

Fig. 1. Grid results for SiO RT models for four of the sample stars. The 1, 2, and 3σ contours in the χ^2 space are shown for ^{28}SiO (red), ^{29}SiO (green), and ^{30}SiO (blue). The thick lines mark the 1σ contours, while the thin lines indicate the 2σ and 3σ contours. The hatched region represents the parameter space where the 1σ contours of the three isotopologues overlap. The squares mark the 'best-fit' models for the three isotopologues. The x-axis ticks show ^{28}SiO abundances. The ^{29}SiO and ^{30}SiO abundances, at each point of the grid, are given by the corresponding ^{28}SiO abundance divided by 20 and 30, respectively (see Sect. 3.2).

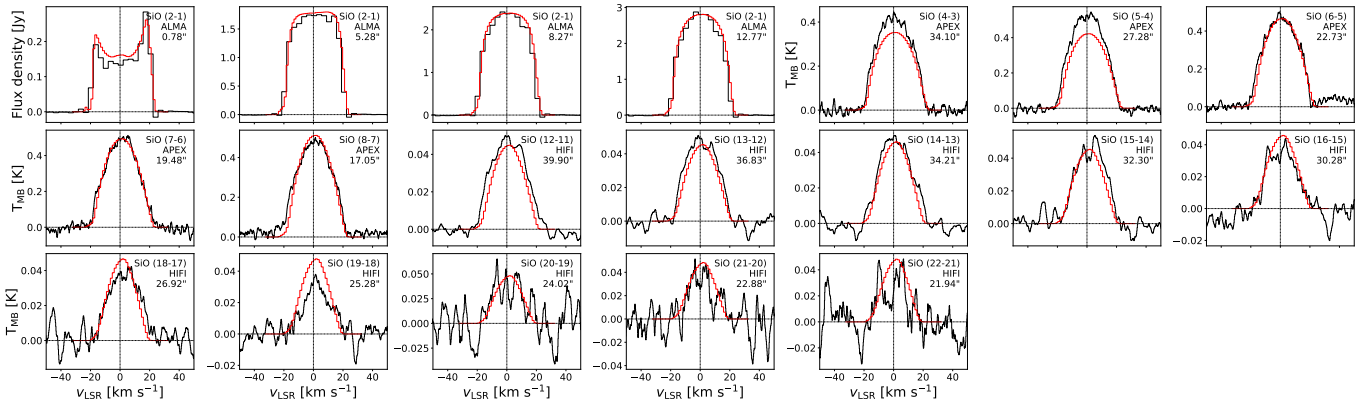

Fig. 2. Observed (black) and modelled (red) SiO line profiles for IRAS 15194−5115. The transition quantum numbers, telescope used, and the beam size (FWHM of the corresponding convolved Gaussian beam (see Sect. 2.2) for the ALMA lines; half power beam width (HPBW) for the SD lines) of the observations are listed in the top right corner of each panel.

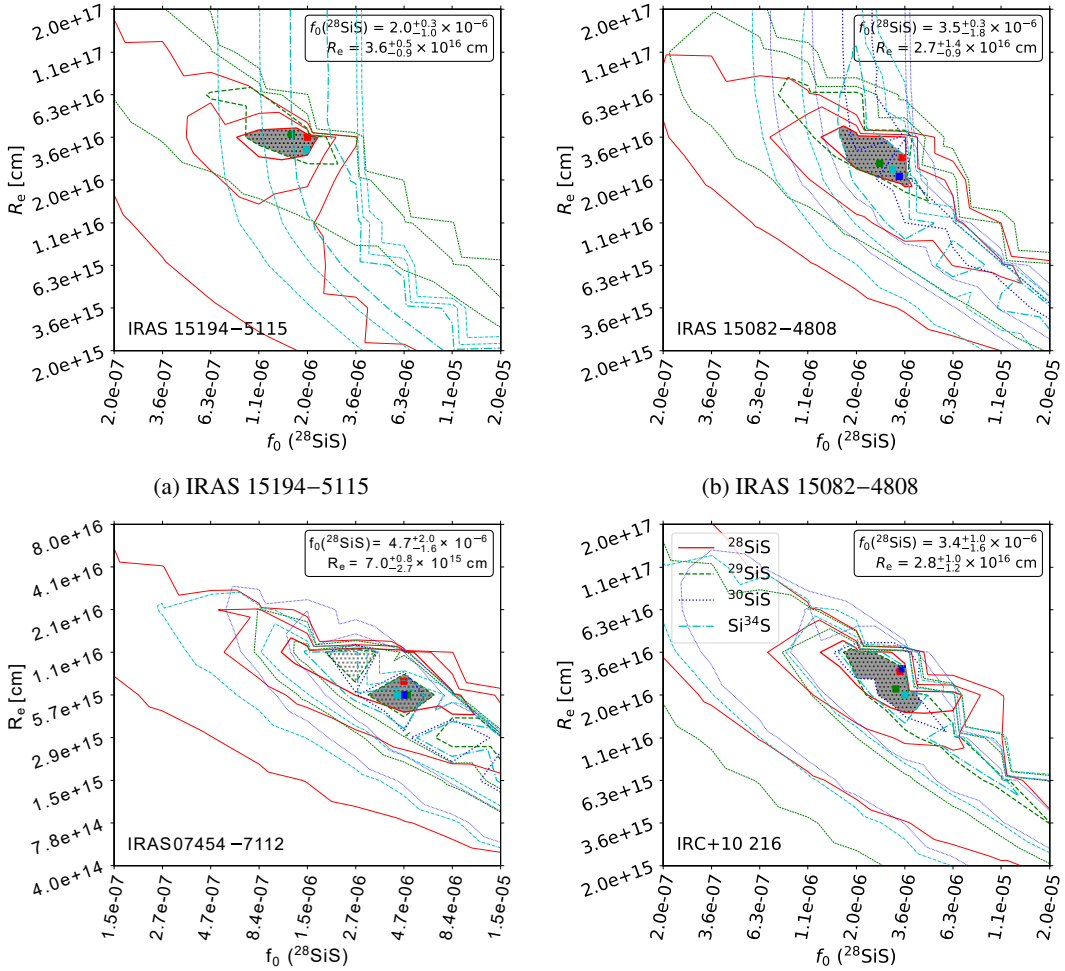

(a) IRAS 15194−5115 (b) IRAS 15082−4808

(c) IRAS 07454−7112 (d) IRC +10 216

Fig. 3. Grid results for SiS RT models for four stars of the sample. As in Fig. 1, but for ^{28}SiS (red), ^{29}SiS (green), ^{30}SiS (blue), and Si^{34}S (cyan). For IRAS 07454−7112, the contours shown are 2, 3, and 4 σ (see Sect. 4.2.3). See Sect. 4.2 for descriptions of the hatched 'best-fit' regions for the individual sources. The x-axis ticks show ^{28}SiS abundances. The ^{29}SiS, ^{30}SiS, and Si^{34}S abundances at each point of the grid are given by its ^{28}SiS abundance divided by 20, 30, and 22, respectively (see Sect. 3.2).

the corresponding CO radial extent, as expected (see Table 2, and Paper II). The grids for the less-abundant isotopologues were designed to have the same R_e sampling as those of the respective main isotopologue grid. These species are photodissociated by radiation across the broadband continuum, and hence do not exhibit differential self-shielding between their isotopologues. The f_0 grids used for the less-abundant isotopologues were obtained by dividing those of the main isotopologues by the respective solar isotopic ratios, i.e. 20 for ^{28}Si/^{29}Si, 30 for ^{28}Si/^{30}Si, and 22 for ^{32}S/^{34}S (Asplund et al. 2009). The grid coverage was manually refined where needed to ensure that the total parameter space explored was adequately spanned and sampled.

4. Results

4.1. SiO

Our models constrain the SiO abundance profiles well for all sources except AFGL 3068, for which no spatially resolved information is available. The χ^2 contour maps for SiO and its studied isotopologues for IRAS 15194−5115, IRAS 15082−4808, IRAS 07454−7112, and IRC +10 216 are shown in Fig. 1. The best-fit ^{28}SiO abundance profiles for the five sources derived from RT modelling are shown in Fig. 10, and the corresponding f_0 and R_e values are given in Table 2. We note that for ^{30}SiO, for all five sources, we only use the J = 4–3 and J = 6–5 lines, as the J = 5–4 line is blended with the Si^{34}S J = 12–11 line. The sections below present the results of the SiO modelling.

4.1.1. IRAS 15194−5115 and IRAS 07454−7112

Models that reproduce the observed ^{28}SiO, ^{29}SiO, and ^{30}SiO emission very well, across both the multi-aperture ALMA spectra and the SD line profiles, were obtained for both IRAS 15194−5115 and IRAS 07454−7112 (Figs. 2, B.1, B.2, B.6, B.7, B.8), yielding well-constrained abundance profiles (Fig. 10). For ^{28}SiO and ^{29}SiO, we have both ALMA and SD lines, whereas for ^{30}SiO, only SD lines are available for these stars. The ^{29}SiO J = 2–1 line displays a sharp peak around ∼3–5 km s^{-1} offset from the systemic velocity on the redshifted side for both sources, possibly caused by substructure within the CSE (Figs. B.1 and B.7). We note that it is unclear whether this could be a maser feature. Maser emission has been detected in the ^{29}SiO

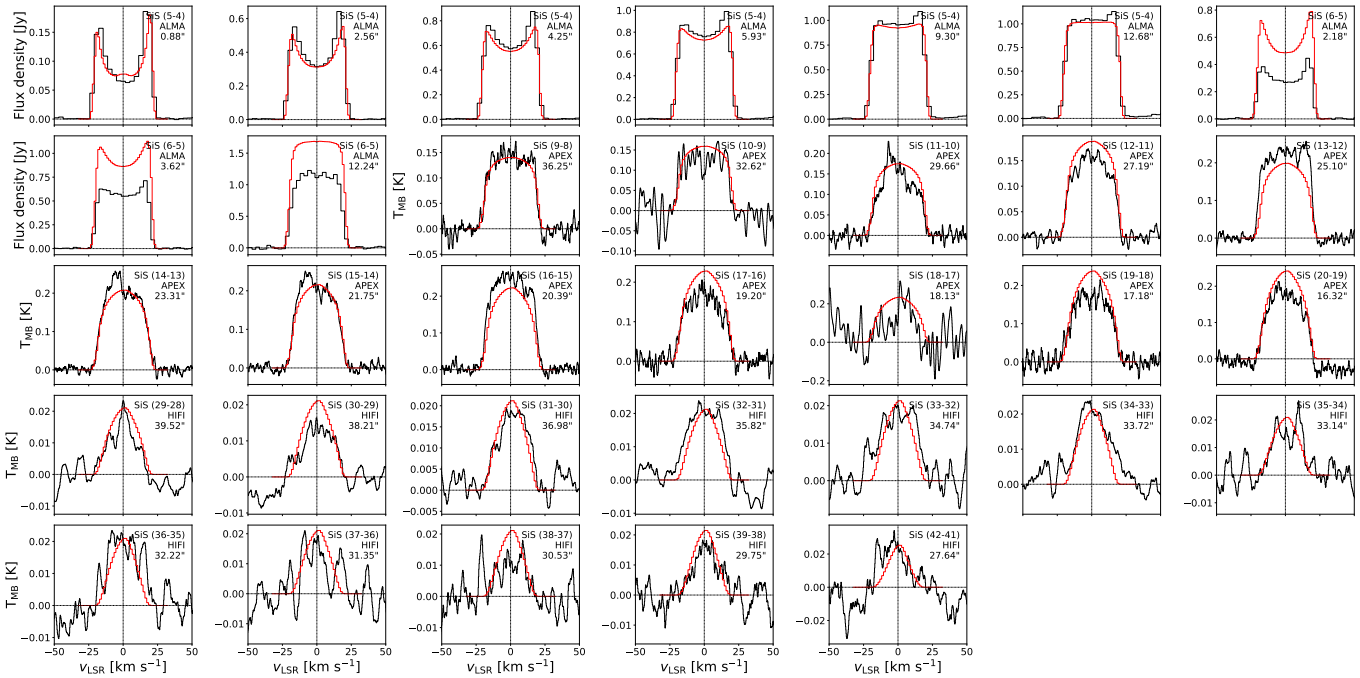

Fig. 4. Observed (black) and modelled (red) SiS line profiles for IRAS 15194−5115. The transition quantum numbers, telescope used, and the beam size (FWHM of the corresponding convolved Gaussian beam (see Sect. 2.2) for the ALMA lines; HPBW for the SD lines) of the observations are listed in the top right corner of each panel.

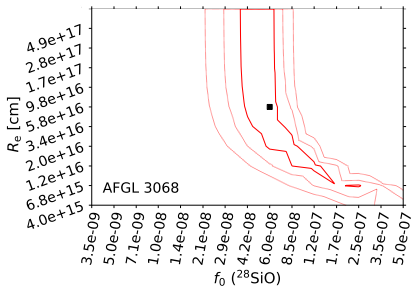

(a) AFGL 3068 - ^{28}SiO

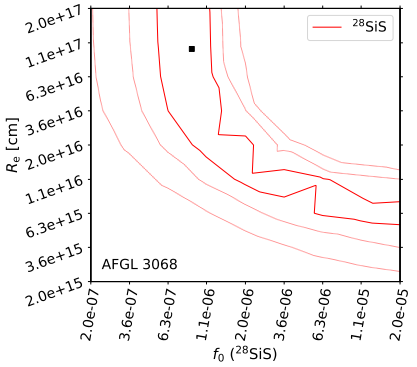

(b) AFGL 3068 - ^{28}SiS

Fig. 5. SiO and SiS grid results for AFGL 3068. The 1, 2, and 3σ contours in the χ^2 space are shown for (a) ^{28}SiO and (b) ^{28}SiS. The degeneracy and lack of strong constraints are due to the non-availability of spatially resolved data (see text). The black square marks the overall 'best-fit' model.

$v = 0, J = 2$–1 line for several M-type stars (e.g. Deguchi et al. 1983; Nguyen-Quang-Rieu et al. 1988), but not so far for carbon stars.

4.1.2. AFGL 3068

For AFGL 3068, we only have 4 SD SiO lines available (Fig. B.9), and no spatially resolved observations, leading to neither f_0 nor R_e being properly constrained (Fig. 5a). We also did not detect any ^{29}SiO and ^{30}SiO lines for this source. We produced modelled line profiles for the non-detected ^{29}SiO and ^{30}SiO $J = 4$–3, 5–4, and 6–5 lines, which fall within the frequency range of our APEX observations, for a single abundance profile obtained by scaling down the derived ^{28}SiO peak abundance (Table 2) by the respective solar isotopic ratios (Table 3), keeping the *e*-folding radius the same. These modelled line intensities were well within the noise of the observed spectra.

4.1.3. IRC +10 216 and IRAS 15082−4808

The SiO $J = 2$–1 line for IRC +10 216 has an asymmetric line profile, with a bump at the redshifted edge, possibly arising from sub-structure within the envelope (see Fig. B.10). For IRC +10 216, and also for IRAS 15082−4808 though to a much smaller extent, we find that the ALMA SiO $J = 2$–1 and the higher-J SiO SD line profiles cannot be fit very well simultaneously. The models that fit the multi-aperture ALMA spectra well always underestimate the higher-J SD lines (see Figs. B.3, B.10), and conversely, the models that fit the higher-J lines tend to overpredict the ALMA $J = 2$–1 line intensities. For IRC +10 216, this issue can also be seen in the models of the less-abundant SiO isotopologues (see Figs. B.11, B.12). For IRAS 15082−4808, this is seen only for the main isotopologue (Fig. B.3), and not for ^{29}SiO and ^{30}SiO which are fit very well by our models (Figs. B.4, B.5).

For IRC +10 216, our best model for the SiO $J = 2$–1 ALMA spectra (see Fig. B.10) underestimates the APEX SiO $J = 4$–3, 5–4, 6–5 lines by ∼40%. While this model fits the IRAM 30 m SD spectrum of the SiO $J = 2$–1 line very well, consistent with its good fit of the $J = 2$–1 ALMA line, it underestimates the other IRAM 30 m lines by ∼20–30%. While this is still

Table 2. Results of RT modelling for the main isotopologues of SiO and SiS.

Source	SiO		SiS	
	f_0	R_e [cm]	f_0	R_e [cm]
IRAS 15194−5115	$1.2^{+0.2}_{-0.5} \times 10^{-6}$	$4.5^{+2.1}_{-0.8} \times 10^{16}$	$2.0^{+0.3}_{-1.0} \times 10^{-6}$	$3.6^{+0.5}_{-0.9} \times 10^{16}$
IRAS 15082−4808	$1.0^{+0.3}_{-0.3} \times 10^{-6}$	$4.2^{+1.6}_{-0.7} \times 10^{16}$	$3.5^{+0.3}_{-1.8} \times 10^{-6}$	$2.7^{+1.4}_{-0.9} \times 10^{16}$
IRAS 07454−7112	$7.1^{+3.2}_{-1.9} \times 10^{-7}$	$1.3^{+0.5}_{-0.3} \times 10^{16}$	$4.7^{+2.0}_{-1.6} \times 10^{-6}$	$7.0^{+0.8}_{-2.7} \times 10^{15}$
AFGL 3068	$6.0^{+\uparrow}_{-\downarrow} \times 10^{-8}$	$5.8^{+\uparrow}_{-\downarrow} \times 10^{16}$	$9.0^{+\uparrow}_{-\downarrow} \times 10^{-7}$	$1.0^{+\uparrow}_{-\downarrow} \times 10^{17}$
IRC +10 216	$2.2^{+1.3}_{-0.9} \times 10^{-7}$	$7.0^{+4.0}_{-1.5} \times 10^{16}$	$3.4^{+1.0}_{-1.6} \times 10^{-6}$	$2.8^{+1.0}_{-1.2} \times 10^{16}$

Notes. f_0: peak abundance, R_e: e-folding radius of the abundance profile. The sub/super-scripts show the uncertainties on the values, and $^{+\uparrow}_{-\downarrow}$ indicates that the uncertainties have not been constrained. We note that the reported uncertainties do not take into account possible uncertainties in the input MLR and distance, which are taken as fixed parameters in the modelling.

Table 3. Isotopic ratios.

Ratio	Species	Source					
		15194−5115	15082−4808	07454−7112	AFGL 3068	IRC +10 216	Solar[(a)]
^{28}Si/^{29}Si	SiO	$22.9^{+8.3}_{-12.4}$	$21.4^{+8.7}_{-10.9}$	$18.7^{+10.3}_{-8.4}$	–	$22.0^{+15.4}_{-19.1}$	20
	SiS	$24.2^{+10.7}_{-15.6}$	$26.1^{+10.3}_{-17.7}$	$19.2^{+10.9}_{-9.8}$	$16.0^{+\uparrow}_{-\downarrow}$	$21.0^{+11.6}_{-12.8}$	
^{28}Si/^{30}Si	SiO	$34.8^{+12.4}_{-19.2}$	$28.1^{+13.3}_{-11.0}$	$27.5^{+15.4}_{-11.8}$	–	$29.1^{+21.6}_{-20.1}$	30
	SiS	–	$31.1^{+16.2}_{-16.9}$	$30.0^{+16.6}_{-16.6}$	$24.0^{+\uparrow}_{-\downarrow}$	$29.2^{+17.1}_{-16.2}$	
^{29}Si/^{30}Si	SiO	$1.5^{+0.7}_{-0.7}$	$1.3^{+0.7}_{-0.5}$	$1.4^{+0.7}_{-0.7}$	–	$1.3^{+1.1}_{-0.9}$	1.5
	SiS	–	$1.2^{+0.8}_{-0.5}$	$1.6^{+0.8}_{-0.9}$	$1.5^{+\uparrow}_{-\downarrow}$	$1.4^{+0.9}_{-0.7}$	
^{32}S/^{34}S	SiS	$22.2^{+11.9}_{-12.0}$	$24.6^{+11.9}_{-14.1}$	$23.7^{+12.4}_{-15.2}$	$18.0^{+\uparrow}_{-\downarrow}$	$20.7^{+12.4}_{-11.2}$	22

Notes. Isotopic ratios are calculated as the ratio of the f_0 values of the best-fit models for the relevant species (Table 2). The sub/super-scripts show the uncertainties on the values, and $^{+\uparrow}_{-\downarrow}$ indicates that the uncertainties have not been constrained. [(a)] Asplund et al. (2009).

within a reasonable range, given the calibration uncertainties of the IRAM 30 m ($\lesssim$30%, see Paper II), it does indicate the possibility of a systematic offset. We note that for IRC +10 216, since the data includes zero-spacing information from the IRAM 30 m OTF maps combined with the ALMA observations (see Sect. 2.3), we do not expect any significant resolved out flux in the emission maps despite the large extent of the emission on the sky. We tried several approaches to address this mismatch in the line fits, as described in Sect. 4.1.4.

4.1.4. Addressing the ALMA – SD fit mismatch

Since our ALMA and SD observations were obtained at different times (see Papers I; II), we checked if SiO lines can be highly variable in carbon star envelopes, and found that the intensity variations are very small for the SiO lines used in this work Cernicharo et al. (2014). So, we cannot attribute the mismatch to variability alone. Also, even if the line intensities are strongly correlated with the stellar light curve, the time delay in receiving the stellar light can be different for different J lines, especially if their excitation regions peak at different radii (see e.g. Fig. 6), an effect that cannot be incorporated into our RT models, which are static. We also tried varying the input stellar luminosity (originally 12 000 $L_\odot$ for IRC +10 216, see Paper II) within the range 5000–16 000 $L_\odot$, but found that this did not affect the modelled line profiles. However, we note that the possible influence of stellar atmospheric bands in the excitation of these lines has not been considered here, as our models describe the central star using only its luminosity and temperature. Using a detailed stellar atmosphere model instead of a blackbody is currently not possible using our RT code.

Emission from the dust also contributes significantly to the circumstellar IR radiation field. We find that changing the dust optical depth affects all line profiles, and not just the relatively higher-J ones. We tested changing the input dust opacities for amorphous carbon grains from those adopted from Suh (2000) (see Paper II) to those of Preibisch et al. (1993), and found that this did not change the modelled line intensities. We note, however, that these two sets of opacities are not widely different. Major changes to the dust opacity, such as turning off the dust radiation field altogether, which we also tested, affect all modelled lines, but do not show significant differential effects between the various transitions (see also Sect. 5.3).

Further, in order to check if the addition of higher vibrational levels than those originally included (see Sect. 3.1) would affect the modelled line intensities by additional IR pumping through higher levels, we tested an SiO molecular description which included levels ranging from v = 0–6. The resulting modelled line profiles match those modelled using only the v = 0, 1 levels within the observational uncertainties.

We also attempted using modified abundance profiles, which had a central step function with a constant abundance f_c out to a radius R_c, followed by the Gaussian profile at larger radii.

Based on our IRC +10 216 model which fits the ALMA SiO J = 2–1 line well (see Table 2 and Fig. 10), we ran a grid of models where the step function abundance in the inner part (f_c) varies between 1.0×10^{-8} and 5.0×10^{-6}, up to radial distances (R_c) in the range 1.0×10^{15}–2.0×10^{16} cm, subsequently followed by the original Gaussian abundance profile at larger radii. The usual logic behind such profiles is that the higher-J lines, such as our SD lines here, are excited closer to the star than the comparatively lower-J lines, such as the ALMA lines in this work, and hence any changes in the fractional abundance in the inner CSE could theoretically impact the intensity of the higher-J lines without significantly affecting the low-J lines (see e.g. Danilovich et al. 2019). However, in our case, this method was also unsuccessful in simultaneously fitting all the ALMA and SD line profiles, as there was no step-function – Gaussian combination which could successfully increase the intensity of the underestimated SD lines without simultaneously forcing the small-aperture ALMA lines to be significantly over-predicted. The implications of this are further discussed in Sect. 5.1.

We also varied the exponent in our input abundance profile description (see Eq. (1)), originally set to 2 for Gaussian profiles. We found that changing this value affects all lines, including the ALMA and SD ones, with the line intensities nominally increasing for increasing values, and hence cannot account for the mismatch seen between the modelled profiles of the different J lines.

None of our IRC +10 216 SiO models that reasonably fit the ALMA lines manages to fit the Yebes SiO J = 1–0 line. Overall, for IRC +10 216, given the incompatibility between the ALMA and SD spectra, we choose to constrain our SiO and isotopologue models using only our ALMA spectra, instead of the SD data, as the ALMA data have much lower calibration uncertainties, and are also all observed at the same time.

4.2. SiS

We were able to successfully constrain the SiS abundances for all sources except AFGL 3068. The χ^2 contour maps for our grids of models for four of the sources, showing the overlaps in the best-fit regions of the different isotopologues, are given in Fig. 3. For IRAS 15194−5115 and IRAS 07454−7112, we have only used the well-constrained ^{28}SiS and ^{29}SiS contours to determine the overlapping best-fit region of the different isotopologues (Figs. 3a, 3c), as the contours of ^{30}SiS and Si^{34}S are not very well constrained (Sections 4.2.1, 4.2.3). For IRAS 15082−4808, the ^{28}SiS, ^{29}SiS, and Si^{34}S contours are used, leaving out the more uncertain ^{30}SiS contours (Fig. 3b, Sect. 4.2.2). For IRC +10 216, where we have well-constrained abundances for all four isotopologues (Sect. 4.2.4), we have used the 1σ contours of all of them to determine the 'best-fit' region in the f_0–R_e parameter space (see Fig. 3b). Fig. 10 shows the best-fit SiS abundance profiles for the sources in our sample. The corresponding f_0 and R_e values are listed in Table 2.

The asymmetric horned profiles seen in the SiS J = 5–4 lines (Figs. 4, B.15, B.19, B.27) for all four sources where we detect the line, are possibly due to weak maser emission (Olofsson et al. 1982; Sahai et al. 1984; Fonfría et al. 2018, e.g.). We note that for all sources, except AFGL 3068 where we do not have ALMA data, the ALMA spectra for the SiS J = 5–4 and 6–5 lines cannot be simultaneously fit, as all models that fit the SiS J = 5–4 line significantly over-predict the SiS J = 6–5 line. The reasons for this are explored in more detail in Sect. 5.2. We also note that while we are able to find models that fit the SiS J = 5–4 ALMA spectra and the available SD lines simultaneously for all sources, there are no models that fit the SiS J = 6–5 ALMA lines and the SD lines together. We therefore choose to constrain our models using the SiS J = 5–4 ALMA line and all available SD lines, and exclude the J = 6–5 lines from this analysis, for all sources.

We note that for Si^{34}S, we do not use the J = 12–11 line to constrain our models as it is blended with the ^{30}SiO J = 5–4 line as mentioned in Sect. 4.1. Further, as done for SiO (see Sect. 4.1.4), we tested an extended SiS dataset including the levels v = 0–5 along with the vibration-rotation transitions with Δv = 1, 2 for the v = 0, 1, and 2 levels, and found that the resulting spectra matched with those modelled using only the v = 0, 1, 2 levels. The following sections describe the SiS modelling results for the different sources.

4.2.1. IRAS 15194−5115

For IRAS 15194−5115, we model the SiS isotopologues ^{28}SiS, ^{29}SiS, and Si^{34}S, but not ^{30}SiS which is not detected towards this source. We find very good fits to the observed line profiles of the different lines for all three modelled isotopologues (see Figs. 4, B.13, B.14), though the uncertainties on the Si^{34}S abundances are not well-constrained (Fig. 3a). For ^{28}SiS and Si^{34}S, our best-fit models over-predict the J = 6–5 line (Figs. 4, B.14). We note that for ^{29}SiS towards this source, we do not have any SD lines available, but only the J = 5–4 and J = 6–5 lines observed using ALMA. Our model overestimates the smallest aperture ALMA line profile for the ^{29}SiS J = 6–5 line, whereas the larger apertures are well fit.

4.2.2. IRAS 15082−4808

Overall, we obtain reasonably well-constrained abundance profiles for this source. We do not have spatially resolved lines for ^{30}SiS for this star, leading us to rely on only the two APEX spectra (Fig. B.17). The ^{30}SiS χ^2 map has broader, less constrained 1σ contours than the other isotopologues, indicating comparatively larger uncertainties (Fig. 3b). The ^{29}SiS J = 5–4 line presents a peculiar line profile with a central spike (Fig. B.16), indicating either maser emission or possibly a blend with the HC_7N v = 0, J = 79–78 line, and is not fit very well by our models.

4.2.3. IRAS 07454−7112

We find models that fit the observed line emission well for all four SiS isotopologues studied for IRAS 07454−7112 (Figs. B.19–B.22). For this source, we use the overlapping region of the 2σ contours of ^{28}SiS and ^{29}SiS to define the best-fit region (see Fig. 3c), as the 1σ contours covered only unrealistically narrow ranges. We find two distinct regions where the contours overlap, but determined by visual inspection of the modelled spectra that the overall line profile fits are better, especially for the SD lines, only for the filled-dotted region towards larger f_0 values, and not the dotted region (Fig. 3c). Therefore, we use only the former area to define our best-fit region for SiS for this source. Our models fit well the ACA spectra for the ^{28}SiS J = 12–11, and the ^{29}SiS J = 13–12 lines, while underestimating the ACA ^{30}SiS J = 19–18 line. We find that ^{28}SiS requires a slightly larger R_e than the other isotopologues for this source (Fig. 3c).

4.2.4. IRC+10 216

For this source, we had two independent spatially resolved observations of the ^{28}SiS J = 5–4 line (see Sect. 2.3). We were able to

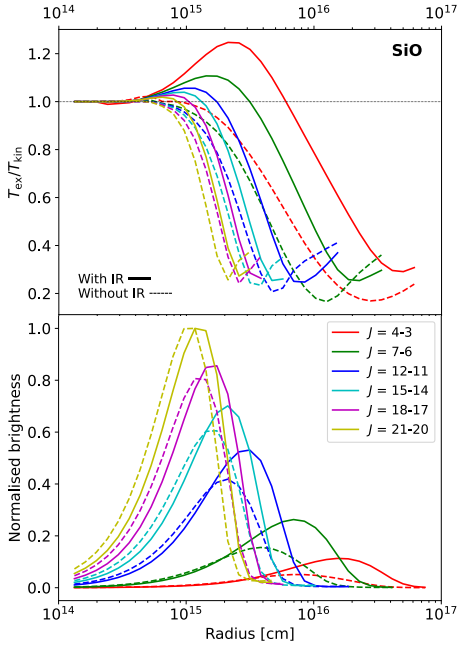

Fig. 6. Ratio of the excitation temperature (T_{ex}) and the kinetic temperature (T_{kin}) for various low- and high-J SiO transitions (top), and their corresponding line-emitting regions (bottom), as functions of radius across the CSE, from the best-fit model for IRAS 15194−5115. The solid lines are from a model that takes into account IR pumping, while the dashed lines are from a model that does not, but is otherwise identical. The line-emitting regions are normalised to the peak of the emitting region of the highest J transition shown.

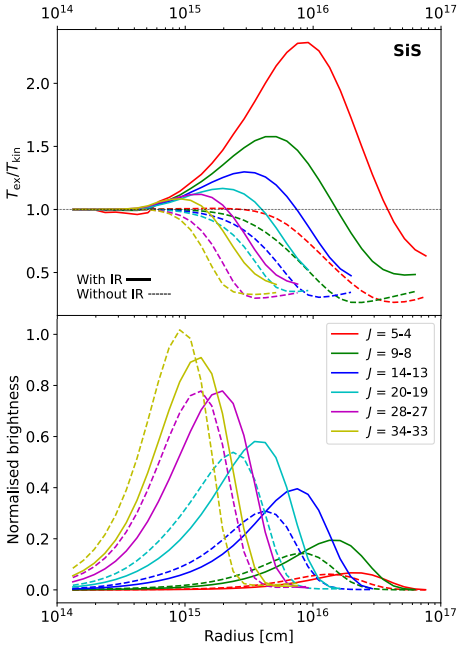

Fig. 7. Same as Fig. 6, but for SiS.

find models that simultaneously fit the multi-aperture spectra for these two lines, as well as a range of SD lines, including APEX observations (J = 9–8 to 14–13) and the Yebes 40 m J = 2–1 line (see Fig. B.27). However, this model overestimates several of the same SiS lines (J = 9–8 to 13–12) and some other higher-J lines (J = 16–15 to 19–18) observed with the IRAM 30 m telescope. However, the IRAM 30 m SiS J = 5–4, 14–13, and 15–14 lines are fitted very well (Fig. B.27).

For the isotopologues ^{29}SiS, ^{30}SiS, and Si^{34}S, for all of which we have both ALMA and SD lines available, our best models fit all available observations, except for some of the smaller apertures in the ALMA multi-aperture spectra for the J = 6–5 lines (see Figs. B.28, B.29, B.30). The observed ALMA J = 5–4 and 6–5 line profiles of ^{29}SiS, ^{30}SiS, and Si^{34}S for IRC +10 216 show a sharp peak around the systemic velocity in the small aperture spectra, which is not visible for larger apertures (see Figs. B.28, B.29, B.30). This is probably formed due to gas velocity variations occurring very close to the star, or sub-structure within the circumstellar envelope. The Si^{34}S J = 5–4 line for this source also presents a horn at the redshifted end of the line profile (Fig. B.30), similar to the one seen in the ^{28}SiS J = 5–4 lines for all our sources (see e.g. Fig. 4).

4.2.5. AFGL 3068

For AFGL 3068, as in the case of SiO, we only have SD lines and no spatially resolved information available. Therefore, the SiS abundance profile of this source is also not well-constrained (see Fig. 5b). However, unlike in the case of SiO, we have SD lines detected for all four SiS isotopologues used, and are able to find models that fit all of them, with similar R_e values (Figs. B.23, B.24, B.25, B.26), and with the abundance ratios matching well with the expected isotopic ratios (see Table 3). This gives more confidence to the derived abundance profiles, though we are not able to determine robust uncertainty ranges in this case, as we do for the other sources.

5. Discussion

We derived the circumstellar fractional abundance profiles of SiO, SiS, and their most abundant isotopologues, for our sample of five carbon stars, by modelling the line emission of these species. Our RT models were constrained using both the radial distribution of the line emission, and information about the excitation conditions traced by different transitions, simultaneously, for all sources except AFGL 3068, for which we did not have interferometric emission maps available. We find models that fit the observations reasonably well for all sources, with a few exceptions as reported in Sect. 4. We derived robust constraints on the SiO and SiS abundance profiles (see Table 2, and Figs. 1, 3) for all sources except AFGL 3068 (see Fig. 5). Overall, our abundance estimates are consistent with previous works based on SD spectra (e.g. Agúndez et al. 2012; Fonfría et al. 2015; Massalkhi et al. 2019, 2024; Schöier et al. 2007) and interferometric observations (e.g. Velilla-Prieto et al. 2019; Schöier et al. 2006). Our poorly constrained SiS abundance profile for AFGL 3068 seems to underestimate the peak abundance and over-predict the e-folding radius, in comparison to SD SiS line modelling results by Schöier et al. (2007). For IRC +10 216, we find an SiO R_e ∼2.5 times larger than those reported by Massalkhi et al. (2024) and Schöier et al. (2006).

Our results show that the SiO abundances for IRAS 15194−5115, IRAS 15082−4808, and IRAS 07454−7112 are consistently larger than that of IRC +10 216, by a factor of ∼3–5, which is significant beyond the 1σ uncertainties of the corresponding models (Table 2). This is in line with the LTE modelling results from Paper I, indicating that simplistic LTE calculations are valid tools for deriving first-order estimates of circumstellar abundances and can reflect underlying trends.

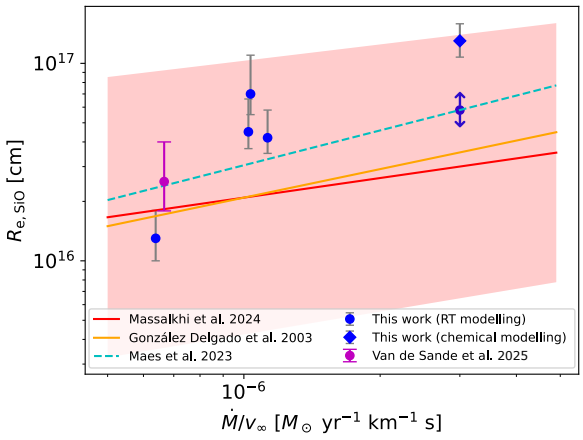

(a) SiO

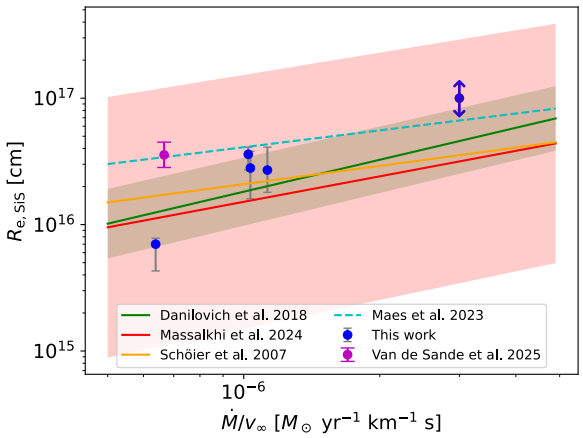

(b) SiS

Fig. 8. R_e of (a) SiO and (b) SiS abundance profiles versus the mass-loss density (ratio of the gas MLR and terminal expansion velocity). The dashed cyan lines are from chemical modelling results (Maes et al. 2023), while the other trends plotted are calculated from RT models. The red and green shaded bands represent the uncertainties on the respective lines. The magenta points are obtained from chemical modelling of a star of MLR 1.0×10^{-5} $M_\odot$ yr^{-1}, and a v_∞ of 15 km s^{-1}, and show the error caused by the uncertainties on the kinetic data (Van de Sande et al. 2025). The rightmost blue circles in both plots are for AFGL 3068, and the open error bars indicate that the R_e is not well-constrained for this source. For SiO, the blue diamond indicates the R_e predicted by our chemical model (see Sect. 5.6).

We find that SiS has ~2–15 times larger initial abundances than SiO (Table 2 and Fig. 9), consistent with the findings of Massalkhi et al. (2019, 2024) who performed RT modelling constrained by SD spectra. This is caused by the fact that the abundance of free O, required to form SiO, is typically low in carbon stars. Further, SiO in general has slightly larger e-folding radii than SiS (Table 2), with both SiO and SiS typically having R_e smaller than that of CS Paper (II). The SiO R_e values are ~55–80% of that of the CS ones, and the SiS R_e are ~30–50% of those of CS (see Paper II). The extents of the molecular emitting regions derived from the azimuthally averaged radial brightness profiles of CS, SiO, and SiS line emission from Paper I also follow the same order, i.e. $R_{out,SiS} < R_{out,SiO} < R_{out,CS}$, where R_{out} denotes the outer radius of the emitting regions, though the observed radial extents of SiO and SiS emission are quite close. The circumstellar gas densities of our sample lie in the range

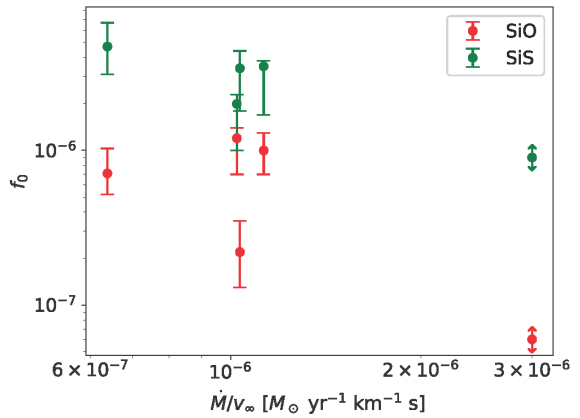

Fig. 9. SiO and SiS peak abundances versus gas densities. The open error bars on the f_0 values for AFGL 3068, marked by arrows, indicate that the abundances for this star have not been well constrained.

6.4×10^{-7}–3.0×10^{-6} $M_\odot$ yr^{-1} km^{-1} s. We note that for lower envelope densities (<10^{-7} $M_\odot$ yr^{-1} km^{-1} s), Massalkhi et al. (2024) found the radial extents of the abundance profiles of SiO to be larger than those of CS.

5.1. Modified SiO abundance profiles

For the case of SiO around IRC +10 216, where we were not able to simultaneously fit the ALMA SiO J = 2–1 and the higher-J SiO SD line profiles, we tried varying the inner abundance using a step function, as described in Sect. 4.1. This technique has been used in the literature (e.g. Schöier et al. 2006, 2007; Danilovich et al. 2019), and works reasonably well in cases where the RT models are constrained either by the radial brightness distribution of a single spatially resolved line, or a small set of SD line profiles relatively close in excitation. However, as described in Sect. 4.1, as we have both spatial information and a large number of SD line profiles tracing different excitation conditions simultaneously available, there are additional constraints in place, particularly for the inner envelope, which is traced by both the small-aperture spectra from the ALMA data (see Sect. 2.2 and Paper II) and the higher-J SD lines. In our case, this leads to not being able to find good models using simple step functions that modify the abundance in the inner regions to fit either the SD line profiles or the small-aperture ALMA spectra, as any such modification to one affects the other as well.

We note that it is indeed possible that the abundance profiles of these species can deviate from a smooth Gaussian, for example, due to depletion onto the dust given their refractory nature, or the presence of radial density variations (see e.g. Cordiner & Millar 2009, Paper I). The presence of a possible binary companion can also alter inner envelope abundances (e.g. Van de Sande & Millar 2022). However, simplistic assumptions such as modifications to the inner abundance alone do not manage to model these effects when stringent observational constraints are placed on the RT models. Addressing these demands RT modelling, possibly in 3D, that properly takes into account not only the observed complex circumstellar density structures such as arcs and possible spirals (see Paper I) and related variations in the gas and dust temperature profiles, but also includes detailed descriptions of the spectral emission from the central star and the dust radiation field, which is beyond the scope of this paper.

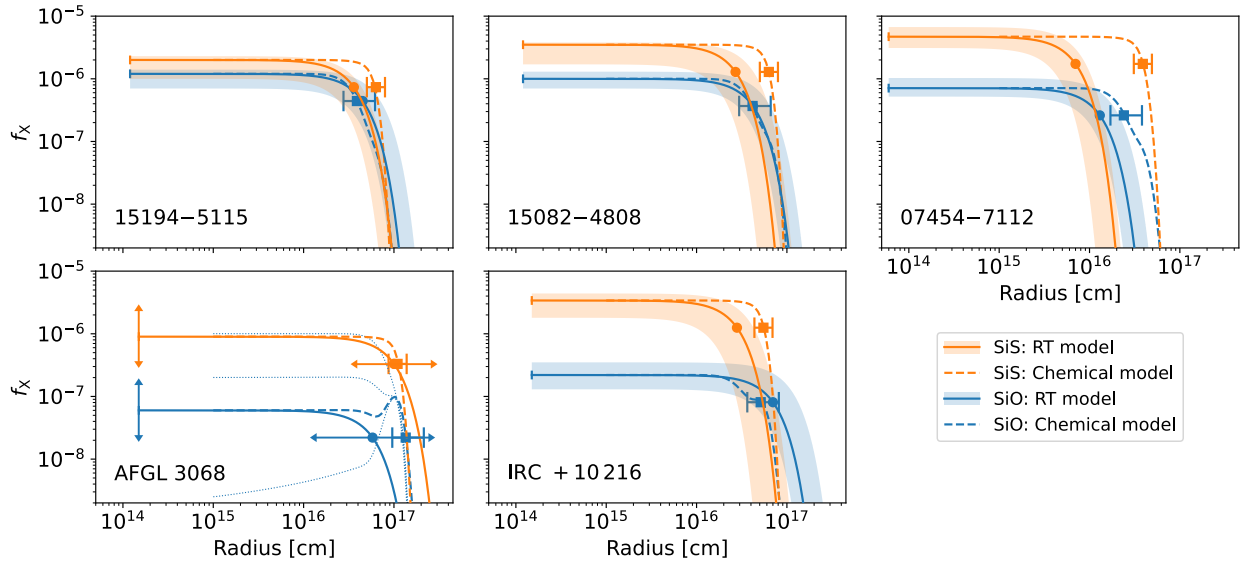

Fig. 10. Comparison of abundance profiles obtained from RT modelling (solid lines with shaded 1σ uncertainties) and chemical modelling (dashed lines) for SiO and SiS. The circles denote the R_e of the respective RT models and the squares mark the R_e of the chemical models. The arrows denote open error bars, indicating that the abundance profile has not been well constrained. The error bars on the chemical model R_e denote the estimated uncertainty in the chemical models based on reaction rate uncertainties (Van de Sande et al. 2025). The blue dotted lines for AFGL 3068 show chemical model abundance profiles with different initial SiO abundances (1.0e-6, 2.0e-7, 2.5e-9).

5.2. A note on SiS J = 6–5

As mentioned in Sect. 4.2, we can not find a model that fits the SiS J = 5–4 and 6–5 lines simultaneously. This issue can be found in the literature as well. The modelled profiles of these two lines for IRC+10 216 by Agúndez et al. (2012) underestimate the J = 5–4 line and marginally overestimate the J = 6–5 line, though in this case these modelled profiles are possibly within the uncertainty of the observed SD line profile. Velilla-Prieto et al. (2019) used two different abundance profiles to fit the SiS J = 5–4 and 6–5 lines for IRC +10 216.

It is known from observations of IRC +10 216 that the SiS J = 5–4 and J = 6–5 lines display anti-correlated intensity variations with the stellar phase (see Carlstrom et al. 1990). It has also been suggested that there are possible IR overlaps between SiS v = 1–0 rovibrational transitions, some also involving the J = 5 level, and those of the ν_5 mode of C_2H_2 and the ν_2 mode of HCN (see e.g. Sahai et al. 1984; Carlstrom et al. 1990; Bieging & Tafalla 1993; Fonfría Expósito et al. 2006; Velilla-Prieto et al. 2019), which can alter the excitation of the J = 5–4 and 6–5 lines. As a quick test, we set the Einstein A-coefficient (A_{ij}) of the SiS v = 1–0, J = 6–5 ro-vibrational transition to zero, to check if this IR pumping route significantly affects the line intensities. We found that this causes significant changes, beyond typical calibration uncertainties, to both the modelled SiS v = 0, J = 5–4 and 6–5 lines. The intensity of the SiS J = 5–4 line increased by ∼30%, and that of the J = 6–5 decreased by ∼25%. This is not to say that it is this specific ro-vibrational transition that is blended with those of other species as discussed above, but only to show that the $v = 0, J = 5$ level is highly sensitive to radiative excitation through the v = 1 levels, indicating that any possible blends that can affect the IR pumping schemes involving this level can significantly alter the line intensities of these v = 0 transitions. Such potential issues of overlaps with the transitions of other molecules in the infrared (IR) ro-vibrational levels (see Sect. 5.2) cannot be directly taken into account in our RT models, which can only include transition information from the species being modelled. Since we find it possible to consistently model our J = 5–4 lines, and not the J = 6–5 lines, with the remaining SD lines across all sources, we chose to keep the J = 5–4 and discard the J = 6–5 from our modelling, in light of the above considerations.

5.3. Radiative excitation

We tested whether radiative excitation via IR pumping (see e.g. Agúndez & Cernicharo 2006; Agúndez et al. 2012; Velilla-Prieto et al. 2019, Paper II) contributes to the line excitation of SiO and SiS. For both molecules, we find that IR pumping significantly affects the line excitation and also the radial distribution of the emission, as also seen for CS in Paper II. The modelled line intensities drop by ∼30–60% for SiO, and ∼30–50% for SiS, when IR pumping is turned off. We note that dust emission is the main source of radiative excitation in these sources, and that the direct contribution of the stellar radiation is comparatively smaller, as found from varying the input stellar luminosities and dust opacities in Sect. 4.1.

Figs. 6 and 7 show the ratio of excitation temperature (T_{ex}) to the gas kinetic temperature (T_{kin}), and the line-emitting regions (see Paper II) for different transitions for SiO and SiS, respectively, from the RT models with and without IR pumping taken into account. The peaks of the emitting regions are shifted inwards when IR pumping is turned off. Beyond the dense inner envelope where the level populations are thermalised ($T_{ex} \approx T_{kin}$), the line excitation becomes increasingly suprathermal ($T_{ex} > T_{kin}$) as we move farther away from the star, as dust provides the IR radiation that radiatively excites the molecules. At the outer parts of the CSE, T_{ex} becomes lower than T_{kin} due to the decrease in gas density and the radiation field intensity.

5.4. Isotopic ratios

We estimated the $^{28}Si/^{29}Si$, $^{28}Si/^{30}Si$, $^{29}Si/^{30}Si$, and $^{32}S/^{34}S$ isotopic ratios from the derived abundances of SiO, SiS and their isotopologues (see Table 3). The calculated ratios are very close

to the solar values for all five sources, as in the case of the $^{32}S/^{34}S$ ratios derived from CS abundances in Paper II. This is expected, as these elements and their isotopes are not produced by nucleosynthesis during the evolution of a star from the main-sequence to the AGB (see Karakas & Lugaro 2016), except for the possible minor enhancement of ^{29}Si and ^{30}Si by the *s*-process during the AGB (see e.g. Zinner et al. 2006; Decin et al. 2010). The proximity of these isotopic ratios to their solar values is also consistent with previous SD estimates (see Peng et al. 2013; He et al. 2008; Cernicharo et al. 2000). For IRAS 07454−7112, we find a $Si^{32}S/Si^{34}S$ abundance ratio of 23.7 (Table 3), which matches well with the solar $^{32}S/^{34}S$ isotopic ratio of 22 (Asplund et al. 2009), in contrast to the considerably lower $Si^{32}S/Si^{34}S$ abundance ratio of 11.4 reported for this star by Danilovich et al. (2018), based on RT modelling of a limited number of SD spectra, including only the J = 10–9 and 11–10 lines of $Si^{34}S$.

We also note that the observed line intensity ratios involving the main isotopologues of SiO and SiS are consistently lower than their corresponding abundance ratios derived from the RT modelling. This is a consequence of the high optical depths in the principal isotopologue lines, as discussed in the case of CS in Paper II.

5.5. Trends with mass-loss density

The mass-loss density (ratio of gas MLR and the terminal gas expansion velocity) serves as a proxy for the circumstellar gas density in the outer regions of the CSE. Our RT modelling results show that the *e*-folding radii of both SiO and SiS increase with this parameter (Fig. 8). This is in line with the empirical trends reported in the literature based on RT models constrained using SD lines (e.g. González Delgado et al. 2003; Schöier et al. 2006; Danilovich et al. 2018; Massalkhi et al. 2024) and chemical models (Maes et al. 2023). Our SiO R_e values appear to follow a slightly sharper rise with density than the trends from the literature, while the increase in our SiS R_e with this density matches very well with previous estimates. We note, however, that these observed trends in this work are influenced by the values for AFGL 3068, which are highly uncertain.

The variation in peak abundances of the two species with mass-loss density is shown in Fig. 9. The SiS peak abundances are consistently larger than those of SiO, as noted earlier. We find no clear correlation between the peak abundances of the two species. Schöier et al. (2006) and Massalkhi et al. (2019) found that SiO, and potentially also SiS abundances, decrease with increasing gas density in carbon star CSEs, based on SD observations of low-J lines. González Delgado et al. (2003) found a similar trend for SiO in M-type AGB stars, and Ramstedt et al. (2009) tentatively found the same trend for S-type stars as well. This is possibly due to the increased adsorption of SiO and SiS onto dust grains at higher densities, caused by elevated collision rates. This indicates that these species, particularly SiO, may play an important role as a gas-phase precursor of dust in AGB stars. Unfortunately, our results cannot confirm or deny these reported trends.

5.6. Chemical modelling

We modelled the chemistry in the CSEs of our sources using a circumstellar chemical model[3] based on the `RATE22` update of the UMIST Database for Astrochemistry (UDfA[4]; Millar et al. 2024). The chemical model used is the same as that in Paper II, a detailed description of which can be found in Millar et al. (2000) and Van de Sande et al. (2018b). We ran individual models for each of our sources, with the input physical parameters customised to match their circumstellar properties as modelled in Paper II, and set the initial abundances of SiO and SiS to those derived from our RT models for each source. The initial abundance of CS was obtained from Paper II, and those of other parent molecules were taken from Agúndez et al. (2020). The resulting chemical model abundance profiles of SiO and SiS are shown in Fig. 10, along with the corresponding abundance profiles derived from RT modelling. Including dust-gas chemistry in these models, to allow for possible changes in the radial gas-phase abundance distributions of our species due to dust-gas interactions, including depletion onto the dust, did not lead to significantly different abundance profiles. No significant depletion of the gas-phase species onto the dust occurs due to the relatively warm dust temperatures (T_c ∼ 1500–1800 K) that we employ as inputs to the RT models, based on our dust modelling results (Paper II).

For SiO, it is seen that the abundance profiles predicted by the chemical model match very well with those from our RT models within the overall uncertainties of the models. This good match between the two abundance profiles shows that the chemical models do a reasonable job in reproducing the radial extent of SiO abundances in carbon star CSEs. This also indicates that our abundance profile for AFGL 3068, which is not well constrained (see Sect. 4), is likely underestimating the SiO *e*-folding radius. To test this, we ran an SiO RT model for AFGL 3068 with the abundance profile predicted by the chemical model, which has a larger R_e than our original RT model, as can be seen from Fig. 10, instead of a typical Gaussian profile. This also yielded reasonable fits to the observed SiO line profiles.

We note that the bump seen at $\sim 10^{17}$ cm in the SiO chemical model abundance profile for AFGL 3068 is due to the reformation of SiO at large radii caused by reactions between H_2O and Si^+, which is produced from SiO by consecutive photoreactions. This bump becomes pronounced only when the initial abundance of SiO is sufficiently low ($\lesssim$2.0e-7), as can be seen from Fig. 10. The same effect can also be seen to a smaller extent in the SiO profile for IRC +10 216, which displays a decrease in the profile at around 3×10^{16} cm, due to the photodissociation of SiO, followed by a small plateau, instead of a continuous decline, due to the above-mentioned reformation.

The chemical model over-predicts the SiS *e*-folding radii for all our sources, except AFGL 3068, where the observations provide a poor constraint (Sect. 4.2.5). This indicates that, in general, SiS is photodissociated more inwards in the CSE than the chemical models predict. While the photodissociation rate of SiO is well known (Heays et al. 2017), that of SiS remains a matter of uncertainty. The results from this work and other studies (Danilovich et al. 2018; Maes et al. 2023; Van de Sande et al. 2025) imply a larger photodissociation rate for SiS, possibly similar to those of CS and SiO, than what is currently assumed in the chemical models. An accurate estimate of its destruction by interstellar photons is needed to fully test model predictions against observational data.

6. Summary and conclusions

We modelled the circumstellar SiO and SiS line emission of a sample of five C-type AGB stars, IRAS 15194−5115, IRAS 15082−4808, IRAS 07454−7112, AFGL 3068, and IRC +10 216, using detailed non-LTE radiative transfer modelling. The models were constrained by a combination of the radial brightness

[3] https://github.com/MarieVdS/rate22_cse_code
[4] https://umistdatabase.uk

distributions from spatially resolved ALMA data, and a number of single-dish spectra from telescopes including APEX, *Herschel*/HIFI, IRAM 30 m, and the Yebes 40 m, tracing a broad range of excitation conditions across the CSE. Though the heterogeneous origin of the datasets used to constrain the models introduces some uncertainty, the modelling overall yielded well-constrained, robust circumstellar fractional abundance profiles for both species and their major isotopologues, except for AFGL 3068, where we could not strictly constrain the abundance profiles due to a lack of spatially resolved observations. We confirmed that SiS has a larger peak abundance in carbon stars compared to SiO. For IRC+10216, our models cannot fit the SiO lower-J ALMA spectra and the higher-J SD spectra simultaneously. Introducing modified abundance profiles with higher abundance in the inner CSE did not solve this problem. We also investigated several other ways to address this issue without success, pointing to the limitations of 1D RT models based on simplistic assumptions about the stars and their circumstellar physical environments.

We find that infrared pumping contributes significantly to the line excitation for both SiO and SiS. The derived SiS peak abundances are very similar across the sample, whereas the SiO abundances of the rest of the sources are a factor of ∼5 larger than that of IRC +10 216. The radial extent estimates of the SiO and SiS abundance profiles increase with circumstellar gas density as expected, though the observed trends are limited by the large uncertainties on the derived values for AFGL 3068. We compared our derived e-folding radii with those predicted by chemical models and found that while they match very well for SiO, the chemical models consistently overestimate the radial extent of SiS. We estimated the ^{28}Si/^{29}Si, ^{28}Si/^{30}Si, ^{29}Si/^{30}Si, and ^{32}S/^{34}S isotopic ratios for our sources, which correspond very well to the respective solar isotopic ratios, as expected.

These results point to the need for spatially resolved information, tracing a broad range of excitation conditions, to robustly constrain circumstellar molecular abundances. Radiative transfer modelling of many different molecular species, constrained by such observations, across a larger sample of AGB stars spanning a broad range of mass-loss rates, in particular sources with lower MLRs than the stars in our sample, complemented by updated chemical models, is needed to produce a comprehensive overview of circumstellar molecular chemistry in carbon stars.

Acknowledgements. The authors sincerely thank the anonymous referee for their constructive feedback, which improved the quality and clarity of this paper. The authors wish to thank P. Bergman for his support in setting up the ALI RT code. We thank M. Agúndez for providing Yebes 40 m and IRAM 30 m SiO and SiS line profiles of IRC +10 216, and J. H. Black for discussions about collisional rates and molecular data files. RU acknowledges data reduction support from the Nordic ALMA Regional Centre (ARC) node based at Onsala Space Observatory (OSO), Sweden. The Nordic ARC node is funded through Swedish Research Council grant No. 2017-00648. We are grateful to D. Tafoya for his continuous support in ALMA data-related tasks. EDB acknowledges financial support from the Swedish National Space Agency. MVdS acknowledges support from the Oort Fellowship at Leiden Observatory. TJM's research at QUB is supported by grant ST/T000198/1 from the STFC. TD is supported in part by the Australian Research Council through a Discovery Early Career Researcher Award (DE230100183). MA acknowledges support from the Olle Engkvist Foundation under project 229-0368. SBC was supported by the NASA Planetary Science Division Internal Scientist Funding Program through the Fundamental Laboratory Research work package (FLaRe). The work of MGR is supported by NOIRLab, which is managed by the Association of Universities for Research in Astronomy (AURA) under a cooperative agreement with the National Science Foundation. This paper makes use of the following ALMA data: ADS/JAO.ALMA#2013.1.00070.S, ADS/JAO.ALMA#2015.1.01271.S, ADS/JAO.ALMA#2017.1.00595.S, ADS/JAO.ALMA#2013.1.00432.S. ALMA is a partnership of ESO (representing its member states), NSF (USA) and NINS (Japan), together with NRC (Canada), MOST and ASIAA (Taiwan), and KASI (Republic of Korea), in cooperation with the Republic of Chile. The Joint ALMA Observatory is operated by ESO, AUI/NRAO and NAOJ. This paper is based on observations with the Atacama Pathfinder EXperiment (APEX) telescope. APEX is a collaboration between the Max Planck Institute for Radio Astronomy, the European Southern Observatory, and the Onsala Space Observatory. Swedish observations on APEX are supported through Swedish Research Council grant No. 2017-00648. The APEX observations were obtained under project numbers O-0107.F-9310 (SEPIA/B5), O-0104.F-9305 (PI230), and O-087.F-9319, O-094.F-9318, O-096.F-9336, and O-098.F-9303 (SHeFI). HIFI has been designed and built by a consortium of institutes and university departments from across Europe, Canada, and the United States (NASA) under the leadership of SRON, Netherlands Institute for Space Research, Groningen, The Netherlands, and with major contributions from Germany, France and the US. Consortium members are Canada: CSA, U. Waterloo; France: CESR, LAB, LERMA, IRAM; Germany: KOSMA, MPIfR, MPS; Ireland: NUI Maynooth; Italy: ASI, IFSI-INAF, Osservatorio Astrofísico di Arcetri-INAF; The Netherlands: SRON, TUD; Poland: CAMK, CBK; Spain: Observatorio Astronómico Nacional (IGN), Centro de Astrobiología (INTA-CSIC); Sweden: Chalmers University of Technology – MC2, RSS & GARD, Onsala Space Observatory, Swedish National Space Board, Stockholm University – Stockholm Observatory; Switzerland: ETH Zurich, FHNW; USA: CalTech, JPL, NHSC. This work is based on observations carried out with the IRAM 30 m and the Yebes 40 m telescopes. IRAM is supported by INSU/CNRS (France), MPG (Germany) and IGN (Spain). The Yebes 40 m telescope at Yebes Observatory is operated by the Spanish Geographic Institute (IGN, Ministerio de Transportes, Movilidad y Agenda Urbana). This research has made use of NASA's Astrophysics Data System (ADS, https://ui.adsabs.harvard.edu). This work made use of Astropy (https://www.astropy.org), a community-developed core Python package and an ecosystem of tools and resources for astronomy (Astropy Collaboration 2013, 2018, 2022). This work has made use of GILDAS (http://www.iram.fr/IRAMFR/GILDAS/) and CASA (https://casa.nrao.edu) software to reduce and analyse data. The computations in this work were run in the Vera HPC cluster using resources provided by C3SE, the Chalmers e-Commons e-Infrastructure group at Chalmers University of Technology, Gothenburg, Sweden.

References

Agúndez, M., & Cernicharo, J. 2006, ApJ, 650, 374
Agúndez, M., Fonfría, J. P., Cernicharo, J., et al. 2012, A&A, 543, A48
Agúndez, M., Cernicharo, J., Quintana-Lacaci, G., et al. 2017, A&A, 601, A4
Agúndez, M., Martínez, J. I., de Andres, P. L., Cernicharo, J., & Martín-Gago, J. A. 2020, A&A, 637, A59
Anand, R. K., Rastogi, S., & Kumar, B. 2023, J. Astrophys. Astron., 44, 47
Andriantsaralaza, M., Ramstedt, S., Vlemmings, W. H. T., et al. 2021, A&A, 653, A53
Andriantsaralaza, M., Ramstedt, S., Vlemmings, W. H. T., & De Beck, E. 2022, A&A, 667, A74
Asplund, M., Grevesse, N., Sauval, A. J., & Scott, P. 2009, ARA&A, 47, 481
Astropy Collaboration (Robitaille, T. P., et al.) 2013, A&A, 558, A33
Astropy Collaboration (Price-Whelan, A. M., et al.) 2018, AJ, 156, 123
Astropy Collaboration (Price-Whelan, A. M., et al.) 2022, ApJ, 935, 167
Bieging, J. H., & Tafalla, M. 1993, AJ, 105, 576
Brunner, M., Danilovich, T., Ramstedt, S., et al. 2018, A&A, 617, A23
Cami, J., Bernard-Salas, J., Peeters, E., & Malek, S. E. 2010, Science, 329, 1180
Carlstrom, U., Olofsson, H., Johansson, L. E. B., Nguyen-Q-Rieu, & Sahai, R. 1990, in From Miras to Planetary Nebulae: Which Path for Stellar Evolution?, eds. M. O. Mennessier, & A. Omont, 170
Cernicharo, J., Guélin, M., & Kahane, C. 2000, A&AS, 142, 181
Cernicharo, J., Teyssier, D., Quintana-Lacaci, G., et al. 2014, ApJ, 796, L21
Cherchneff, I. 2012, A&A, 545, A12
Cordiner, M. A., & Millar, T. J. 2009, ApJ, 697, 68
Danilovich, T., Ramstedt, S., Gobrecht, D., et al. 2018, A&A, 617, A132
Danilovich, T., Richards, A. M. S., Karakas, A. I., et al. 2019, MNRAS, 484, 494
Dayou, F., & Balança, C. 2006, A&A, 459, 297
Decin, L., De Beck, E., Brünken, S., et al. 2010, A&A, 516, A69
Deguchi, S., Good, J., Fan, Y., et al. 1983, ApJ, 264, L65
Endres, C. P., Schlemmer, S., Schilke, P., Stutzki, J., & Müller, H. S. P. 2016, J. Mol. Spectrosc., 327, 95
Fonfría, J. P., Cernicharo, J., Richter, M. J., et al. 2015, MNRAS, 453, 439
Fonfría, J. P., Fernández-López, M., Pardo, J. R., et al. 2018, ApJ, 860, 162
Fonfría Expósito, J. P., Agúndez, M., Tercero, B., Pardo, J. R., & Cernicharo, J. 2006, ApJ, 646, L127
Gong, Y., Henkel, C., Spezzano, S., et al. 2015, A&A, 574, A56
González Delgado, D., Olofsson, H., Kerschbaum, F., et al. 2003, A&A, 411, 123
He, J. H., Dinh-V-Trung, Kwok, S., et al. 2008, ApJS, 177, 275
Heays, A. N., Bosman, A. D., & van Dishoeck, E. F. 2017, A&A, 602, A105

Höfner, S., & Olofsson, H. 2018, A&A Rev., 26, 1
Karakas, A. I., & Lugaro, M. 2016, ApJ, 825, 26
Kobayashi, C., Karakas, A. I., & Umeda, H. 2011, MNRAS, 414, 3231
Maercker, M., Schöier, F. L., Olofsson, H., Bergman, P., & Ramstedt, S. 2008, A&A, 479, 779
Maes, S., Van de Sande, M., Danilovich, T., De Ceuster, F., & Decin, L. 2023, MNRAS, 522, 4654
Massalkhi, S., Agúndez, M., & Cernicharo, J. 2019, A&A, 628, A62
Massalkhi, S., Agúndez, M., Fonfría, J. P., et al. 2024, A&A, 688, A16
Matsuura, M., Barlow, M. J., Zijlstra, A. A., et al. 2009, MNRAS, 396, 918
Millar, T. J., Herbst, E., & Bettens, R. P. A. 2000, MNRAS, 316, 195
Millar, T. J., Walsh, C., Van de Sande, M., & Markwick, A. J. 2024, A&A, 682, A109
Müller, H. S., Schlöder, F., Stutzki, J., & Winnewisser, G. 2005, J. Mol. Struct., 742, 215
Nguyen-Quang-Rieu, Deguchi, S., Izumiura, H., et al. 1988, ApJ, 330, 374
Olofsson, H., Johansson, L. E. B., Hjalmarson, A., & Nguyen-Quang-Rieu. 1982, A&A, 107, 128
Pardo, J. R., Cernicharo, J., Tercero, B., et al. 2022, A&A, 658, A39
Patel, N. A., Young, K. H., Gottlieb, C. A., et al. 2011, ApJS, 193, 17
Peng, T.-C., Humphreys, E. M. L., Testi, L., et al. 2013, A&A, 559, L8
Pickett, H. M., Poynter, R. L., Cohen, E. A., et al. 1998, J. Quant. Spec. Radiat. Transf., 60, 883
Preibisch, T., Ossenkopf, V., Yorke, H. W., & Henning, T. 1993, A&A, 279, 577
Ramstedt, S., Schöier, F. L., & Olofsson, H. 2009, A&A, 499, 515
Ramstedt, S., Vlemmings, W. H. T., Doan, L., et al. 2020, A&A, 640, A133
Sahai, R., Wootten, A., & Clegg, R. E. S. 1984, ApJ, 284, 144
Schöier, F. L., Olofsson, H., & Lundgren, A. A. 2006, A&A, 454, 247
Schöier, F. L., Bast, J., Olofsson, H., & Lindqvist, M. 2007, A&A, 473, 871
Siebert, M. A., Van de Sande, M., Millar, T. J., & Remijan, A. J. 2022, ApJ, 941, 90
Suh, K.-W. 2000, MNRAS, 315, 740
Tielens, A. G. G. M. 2005, The Physics and Chemistry of the Interstellar Medium
Tielens, A. G. G. M. 2008, ARA&A, 46, 289
Tuo, J., Li, X., Sun, J., et al. 2024, ApJS, 271, 45
Unnikrishnan, R., De Beck, E., Nyman, L. Å., et al. 2024, A&A, 684, A4
Unnikrishnan, R., Andriantsaralaza, M., De Beck, E., et al. 2025, A&A, 699, A48
Van de Sande, M., & Millar, T. J. 2022, MNRAS, 510, 1204
Van de Sande, M., Decin, L., Lombaert, R., et al. 2018a, A&A, 609, A63
Van de Sande, M., Sundqvist, J. O., Millar, T. J., et al. 2018b, A&A, 616, A106
Van de Sande, M., Walsh, C., Mangan, T. P., & Decin, L. 2019, MNRAS, 490, 2023
Van de Sande, M., Walsh, C., & Millar, T. J. 2023, Faraday Discuss., 245, 586
Van de Sande, M., Gueguen, M., Danilovich, T., & Millar, T. J. 2025, MNRAS, accepted [arXiv:2511.13638]
Velilla Prieto, L., Cernicharo, J., Quintana-Lacaci, G., et al. 2015, ApJ, 805, L13
Velilla-Prieto, L., Cernicharo, J., Agúndez, M., et al. 2019, A&A, 629, A146
Woods, P. M., Schöier, F. L., Nyman, L. Å., & Olofsson, H. 2003, A&A, 402, 617
Zeichner, S. S., Aponte, J. C., Bhattacharjee, S., et al. 2023, Science, 382, 1411
Zinner, E., Nittler, L. R., Gallino, R., et al. 2006, ApJ, 650, 350

Appendix A: Observed line intensities

Table A.1: SiO lines used in this work.

Transition	Rest Frequency [GHz]	E_{up} [K]	Telescope	Integrated Intensity [Jy km s^{-1} for ALMA and ACA; K km s^{-1} for others]				
				15194−5115	15082−4808	07454−7112	AFGL 3068	IRC +10 216
1 – 0	43.423853	2.08	Yebes	–	–	–	–	15.4[(b)]
2 – 1	86.846985	6.25	ALMA	96.1	35.1	15.8	–	422.5[(c)]
			IRAM	–	–	–	–	65.2[(d)]
3 – 2	130.268683	12.50	IRAM	–	–	–	–	139.4[(d)]
4 – 3	173.688238	20.84	APEX	12.4	1.2	2.4	0.9	62.1
			IRAM	–	–	–	–	226.4[(d)]
5 – 4	217.104919	31.26	APEX	15.2	1.2	3.6	0.9	75.4
			IRAM	–	–	–	–	248.2[(d)]
			ACA	–	–	97.5[(a)]	23.1[(a)]	–
6–5	260.518009	43.76	APEX	13.6	1.2	4.2	0.9	89.9
			IRAM	–	–	–	–	281.4[(d)]
7 – 6	303.926812	58.35	APEX	13.8	–	–	–	–
			IRAM	–	–	–	–	349.9[(d)]
8 – 7	347.330581	75.02	APEX	14.4	–	–	–	–
			IRAM	–	–	–	–	380.6[(d)]
12 – 11	520.881187	162.52	HIFI	1.4	–	–	–	–
13 – 12	564.249098	189.60	HIFI	1.3	–	–	–	–
14 – 13	607.607719	218.76	HIFI	1.3	–	–	–	–
15 – 14	650.956290	250.00	HIFI	1.2	–	–	–	–
16 – 15	694.294114	283.32	HIFI	0.9	–	–	–	–
18 – 17	780.934648	356.20	HIFI	0.5	–	–	–	–
19 – 18	824.235900	395.75	HIFI	0.4	–	–	–	–
20 – 19	867.523546	437.39	HIFI	0.4	–	–	–	–
21 – 20	910.796851	481.10	HIFI	0.8	–	–	–	–
22 – 21	954.055103	526.89	HIFI	0.6	–	–	–	–

Notes. The ALMA and APEX lines reported for IRAS 15194−5115, IRAS 15082−4808, and IRAS 07454−7112 are from Paper I, unless otherwise specified. All HIFI lines listed are from our *Herschel*/HIFI spectral survey of IRAS 15194−5115 (see Paper I). For the ALMA (and ACA) lines, the integrated intensity values reported are in units of Jy km s^{-1} and are calculated using spectra extracted from apertures large enough to encompass all detected line emission. For all other SD observations (APEX, HIFI, IRAM, Yebes), the integrated intensities are given in units of K km s^{-1}, in the main beam ($T_{\rm MB}$) temperature scale. The relevant beam size ranges and main beam efficiencies for the SD telescopes are described in Paper II, and the individual beam sizes at each transition frequency are indicated in Fig. 2 and the relevant figures in Appendix B, alongside the corresponding line spectra. [(a)] The DEATHSTAR ACA survey (Ramstedt et al. 2020; Andriantsaralaza et al. 2021); [(b)] Massalkhi et al. (2024); [(c)] Velilla-Prieto et al. (2019); [(d)] Agúndez et al. (2012).

Table A.2: ^{29}SiO lines used in this work.

Transition	Rest Frequency [GHz]	E_{up} [K]	Telescope	Integrated Intensity [Jy km s^{-1} for ALMA and ACA; K km s^{-1} for others]				
				15194−5115	15082−4808	07454−7112	AFGL 3068	IRC +10 216
2 – 1	85.759199	6.17	ALMA	9.8	2.5	1.3	–	31.1[(c)]
4 – 3	171.512802	20.58	APEX	1.2	0.5	0.3	–	5.4
5 – 4	214.385757	30.87	APEX	1.6	0.5	0.4	–	7.1
6–5	257.255215	43.21	APEX	1.5	0.5	0.4	–	6.9
7 – 6	300.120477	57.62	APEX	1.3	–	–	–	–
8 – 7	342.980842	74.08	APEX	1.1	–	–	–	–
			ACA	–	–	17.5[(a)]	–	–
12 – 11	514.359357	160.48	HIFI	0.1	–	–	–	–

Notes. As in Table. A.1, but for ^{29}SiO.

Table A.3: ^{30}SiO lines used in this work.

Transition	Rest Frequency [GHz]	E_{up} [K]	Telescope	Integrated Intensity [Jy km s^{-1} for ALMA and ACA; K km s^{-1} for others]				
				15194−5115	15082−4808	07454−7112	AFGL 3068	IRC +10 216
2 – 1	169.486877	20.34	ALMA	–	–	–	–	23.1[c]
4 – 3	169.486877	20.34	APEX	0.7	0.3	0.2	–	3.7
5 – 4	211.853474	30.50	APEX	1.5	0.6	0.5	–	13.2
6–5	254.216656	42.70	APEX	1.0	0.4	0.3	–	5.5
7 – 6	296.575740	56.94	APEX	0.9	–	–	–	–
8 – 7	338.930044	73.20	APEX	1.1	–	–	–	–

Notes. As in Table. A.1, but for ^{30}SiO.

Table A.4: SiS lines used in this work.

Transition	Rest Frequency [GHz]	E_{up} [K]	Telescope	Integrated Intensity [Jy km s^{-1} for ALMA and ACA; K km s^{-1} for others]				
				15194−5115	15082−4808	07454−7112	AFGL 3068	IRC +10 216
2 – 1	36.309627	2.61	Yebes	–	–	–	–	9.1[b]
5 – 4	90.771564	13.07	ALMA	43.8	23.1	12.1	–	645.4[c], 673.0[e]
			IRAM	–	–	–	–	121.3[d]
6–5	108.924301	18.30	ALMA	45.8	27.0	14.9	–	653.7[c]
			IRAM	–	–	–	–	116.2[d]
8 – 7	145.227053	31.37	IRAM	–	–	–	–	289.3[d]
9 – 8	163.376785	39.21	APEX	5.2	3.8	2.3	2.4	96.7
			IRAM	–	–	–	–	370.0[d]
10 – 9	181.525218	47.92	APEX	4.9	2.9	2.0	1.9	83.5
			IRAM	–	–	–	–	272.0[d]
11 – 10	199.672229	57.50	APEX	5.2	4.1	2.4	2.2	99.7
			IRAM	–	–	–	–	368.8[d]
12 – 11	217.817663	67.95	APEX	5.2	3.9	3.1	3.3	114.7
			IRAM	–	–	–	–	302.8[d]
			ACA	–	–	85.3[a]	89.6[a]	–
13 – 12	235.961363	79.28	APEX	8.7	4.6	3.9	3.5	136.4
			IRAM	–	–	–	–	406.6[d]
14 – 13	254.103210	91.47	APEX	7.3	4.1	4.7	3.1	137.4
			IRAM	–	–	–	–	591.4[d]
15 – 14	272.243052	104.54	APEX	7.2	–	–	–	–
			IRAM	–	–	–	–	654.8[d]
16 – 15	290.380757	118.47	APEX	8.8	–	5.0[f]	–	–
			IRAM	–	–	–	–	613.2[d]
17 – 16	308.516143	133.28	APEX	5.5	–	–	–	–
			IRAM	–	–	–	–	381.8[d]
18 – 17	326.649109	148.96	APEX	3.7	–	–	–	–
			IRAM	–	–	–	–	522.7[d]
19 – 18	344.779481	165.50	APEX	5.7	–	7.7[f]	–	–
			IRAM	–	–	–	–	471.5[d]
20 – 19	362.907164	182.92	APEX	5.3	–	–	–	–
29 – 28	525.909965	378.80	HIFI	0.4	–	–	–	–
30 – 29	544.002518	404.90	HIFI	0.4	–	–	–	–
31 – 30	562.090777	431.88	HIFI	0.3	–	–	–	–
32 – 31	580.174604	459.72	HIFI	0.6	–	–	–	–
33 – 32	598.253828	488.43	HIFI	0.4	–	–	–	–
34 – 33	616.328337	518.01	HIFI	0.6	–	–	–	–
35 – 34	634.397967	548.46	HIFI	0.7	–	–	–	–
36 – 35	652.462584	579.77	HIFI	0.6	–	–	–	–
37 – 36	670.522052	611.95	HIFI	0.4	–	–	–	–
38 – 37	688.576198	645.00	HIFI	0.3	–	–	–	–
39 – 38	706.624908	678.91	HIFI	0.4	–	–	–	–
42 – 41	760.736942	785.84	HIFI	0.6	–	–	–	–

Notes. As in Table. A.1, but for SiS. [e] ALMA project 2015.1.01271.S (PI: D. Keller), [f] Danilovich et al. (2018).

Table A.5: ^{29}SiS lines used in this work.

Transition	Rest Frequency [GHz]	E_{up} [K]	Telescope	Integrated Intensity [Jy km s^{-1} for ALMA and ACA; K km s^{-1} for others]				
				15194−5115	15082−4808	07454−7112	AFGL 3068	IRC +10 216
5 – 4	89.103749	12.83	ALMA	2.5	1.7	0.4	–	23.9[c]
6–5	106.922980	17.96	ALMA	3.5	–	1.1	–	48.9[c]
9 – 8	160.375151	38.49	APEX	–	–	–	0.2	6.9
10 – 9	178.190241	47.04	APEX	–	–	–	–	6.6
11 – 10	196.003949	56.44	APEX	–	0.3	–	–	–
12 – 11	213.816140	66.71	APEX	–	0.2	0.2	0.3	8.6
13 – 12	231.626673	77.82	APEX	–	0.2	0.3	0.3	10.1
			ACA	–	–	8.2[a]	8.3[a]	–
14 – 13	249.435412	89.79	APEX	–	0.2	0.3	0.3	9.6
15 – 14	267.242218	102.62	APEX	–	–	0.4	0.4	10.6

Notes. As in Table. A.1, but for ^{29}SiS.

Table A.6: ^{30}SiS lines used in this work.

Transition	Rest Frequency [GHz]	E_{up} [K]	Telescope	Integrated Intensity [Jy km s^{-1} for ALMA and ACA; K km s^{-1} for others]				
				15194−5115	15082−4808	07454−7112	AFGL 3068	IRC +10 216
5 – 4	87.550558	12.61	APEX	–	–	–	–	20.6[c]
6–5	105.059203	17.65	APEX	–	–	0.6	–	31.3[c]
10 – 9	175.084456	46.22	APEX	–	–	–	–	4.5
11 – 10	192.587770	55.46	APEX	–	–	–	–	5.1
12 – 11	210.089618	65.54	APEX	–	0.1	0.2	0.2	6.3
13 – 12	227.589867	76.47	APEX	–	0.2	0.2	0.2	6.4
14 – 13	245.088383	88.23	APEX	–	–	0.1	0.2	5.5
15 – 14	262.585034	100.83	APEX	–	–	0.2	0.2	5.5
19 – 18	332.550309	159.63	ACA	–	–	12.4[a]	9.7[a]	–

Notes. As in Table. A.1, but for ^{30}SiS.

Table A.7: Si^{34}S lines used in this work.

Transition	Rest Frequency [GHz]	E_{up} [K]	Telescope	Integrated Intensity [Jy km s^{-1} for ALMA and ACA; K km s^{-1} for others]				
				15194−5115	15082−4808	07454−7112	AFGL 3068	IRC +10 216
5 – 4	88.285828	12.71	ALMA	–	1.0	0.4	–	19.0[c]
6–5	105.941503	17.80	ALMA	1.9	–	0.7	–	34.6[c]
9 – 8	158.903106	38.13	APEX	–	–	–	–	6.2
10 – 9	176.554715	46.61	APEX	–	–	–	–	6.0
11 – 10	194.204969	55.93	APEX	–	–	–	0.2	7.5
13 – 12	229.500868	77.11	APEX	–	0.3	0.2	0.2	8.8
14 – 13	247.146242	88.97	APEX	–	0.2	0.3	0.3	8.4
15 – 14	264.789719	101.68	APEX	–	0.3	0.3	0.3	8.9
16 – 15	282.431163	115.23	APEX	0.5	–	–	–	–

Notes. As in Table. A.1, but for Si^{34}S.

Appendix B: SiO and SiS line fits

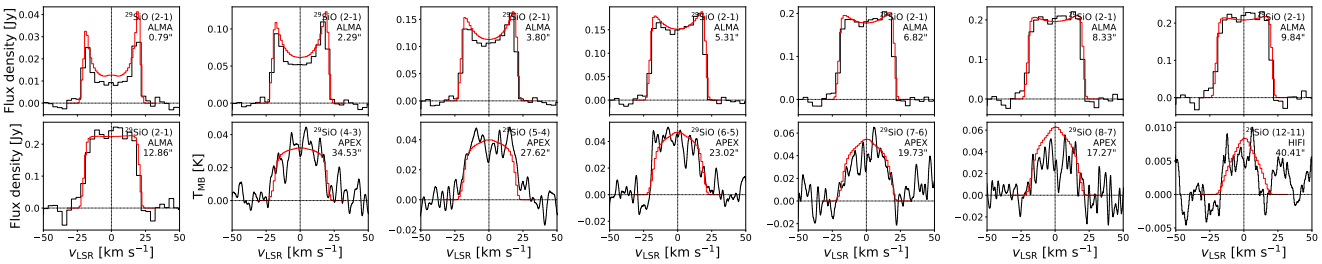

Fig. B.1: Observed (black) and modelled (red) ^{29}SiO line profiles for IRAS 15194-5115. The transition quantum numbers, telescope used, and the beam size (FWHM of the corresponding convolved Gaussian beam (see Sect. 2.2) for the ALMA lines; HPBW for the SD lines) of the observations are listed in the top right corner of each panel.

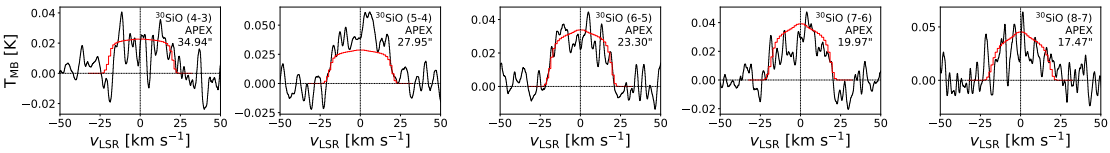

Fig. B.2: As in Fig. B.1, but for IRAS 15194-5115, ^{30}SiO

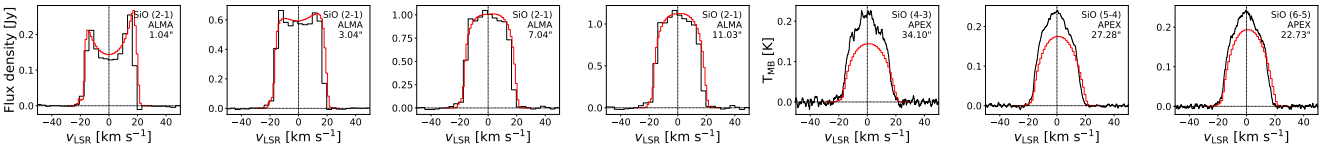

Fig. B.3: As in Fig. B.1, but for IRAS 15082-4808, SiO

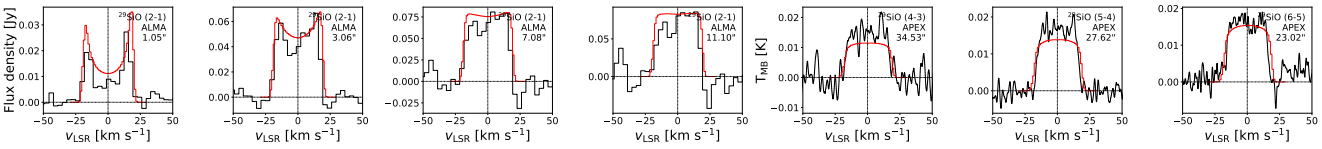

Fig. B.4: As in Fig. B.1, but for IRAS 15082-4808, ^{29}SiO

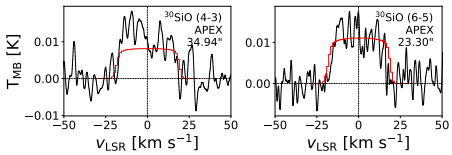

Fig. B.5: As in Fig. B.1, but for IRAS 15082-4808, ^{30}SiO

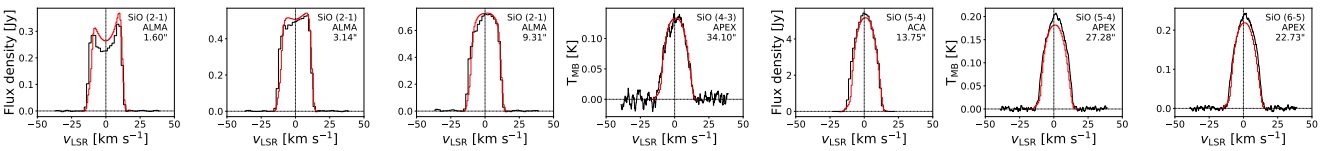

Fig. B.6: As in Fig. B.1, but for IRAS 07454-7112, SiO

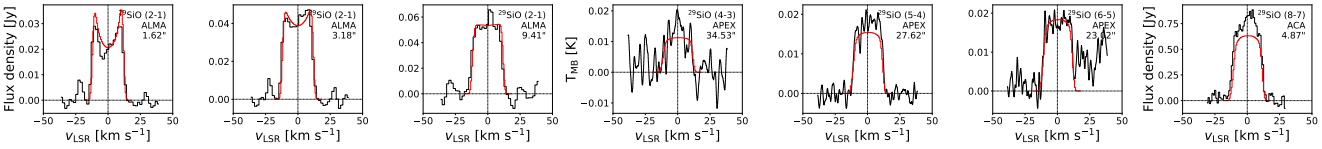

Fig. B.7: As in Fig. B.1, but for IRAS 07454-7112, ^{29}SiO

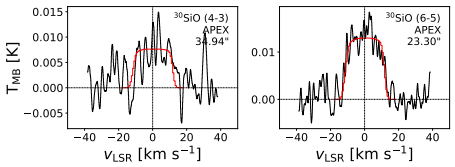

Fig. B.8: As in Fig. B.1, but for IRAS 07454-7112, ^{30}SiO

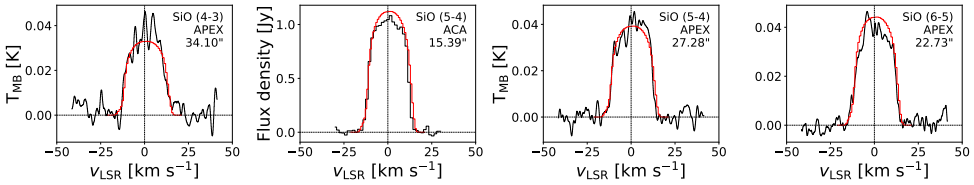

Fig. B.9: As in Fig. B.1, but for AFGL 3068, SiO

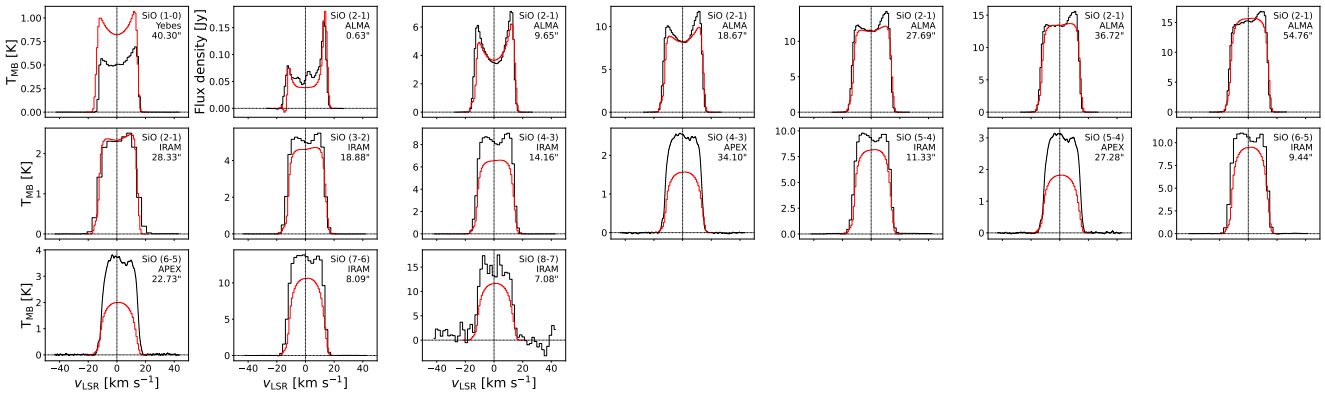

Fig. B.10: As in Fig. B.1, but for IRC+10216, SiO

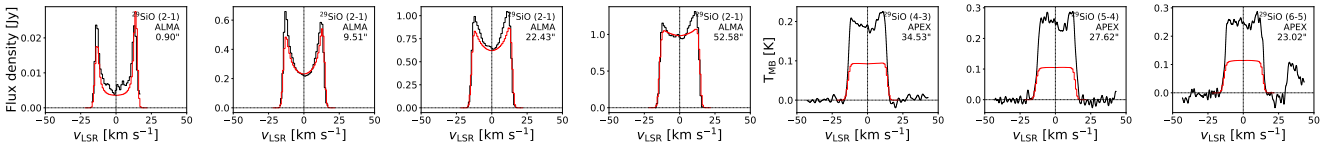

Fig. B.11: As in Fig. B.1, but for IRC+10216, ^{29}SiO

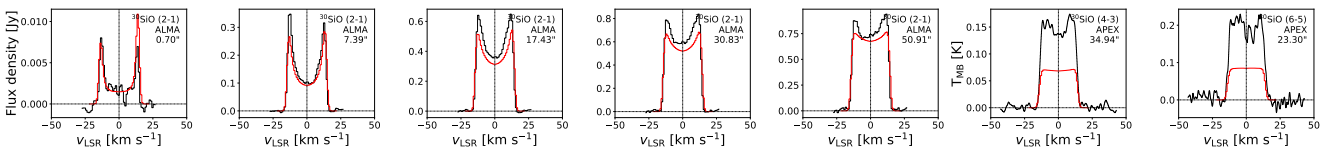

Fig. B.12: As in Fig. B.1, but for IRC+10216, ^{30}SiO

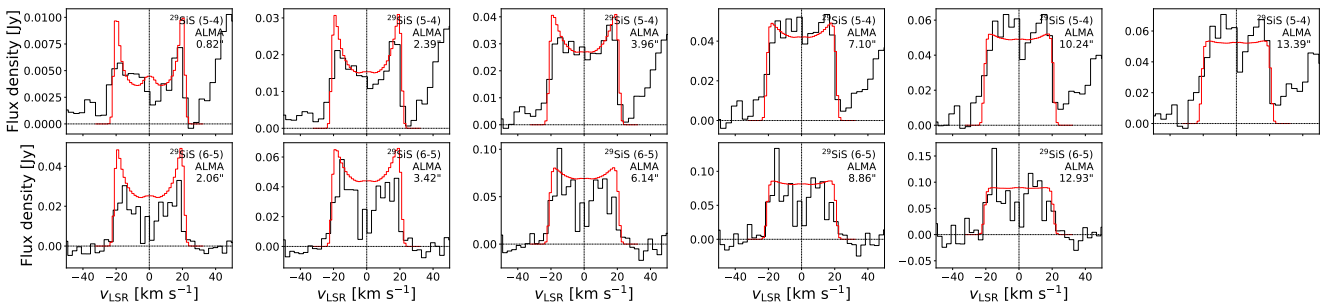

Fig. B.13: As in Fig. B.1, but for IRAS 15194-5115, ^{29}SiS

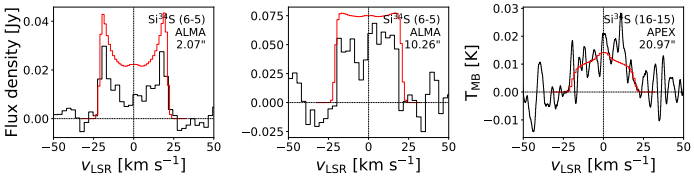

Fig. B.14: As in Fig. B.1, but for IRAS 15194-5115, Si^{34}S

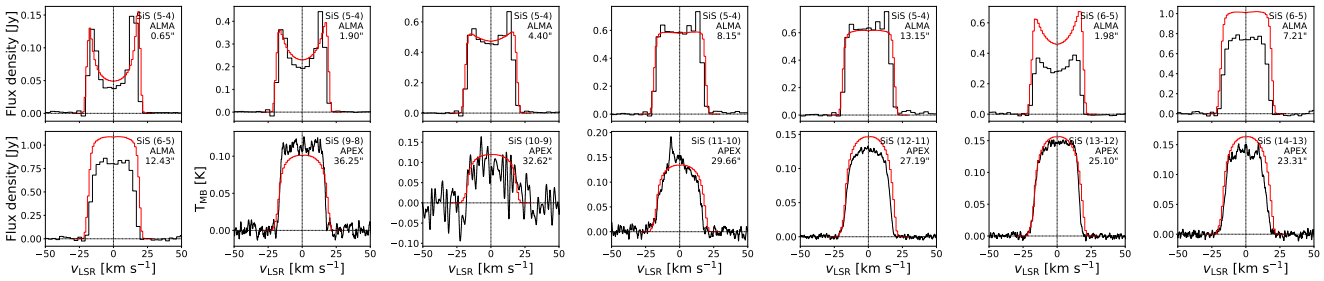

Fig. B.15: As in Fig. B.1, but for IRAS 15082-4808, SiS

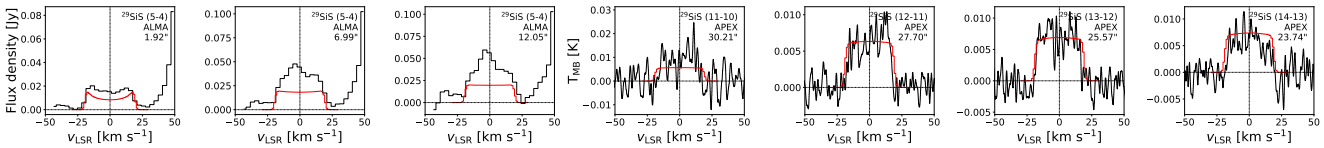

Fig. B.16: As in Fig. B.1, but for IRAS 15082-4808, ^{29}SiS

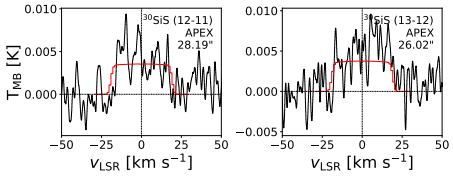

Fig. B.17: As in Fig. B.1, but for IRAS 15082-4808, ^{30}SiS

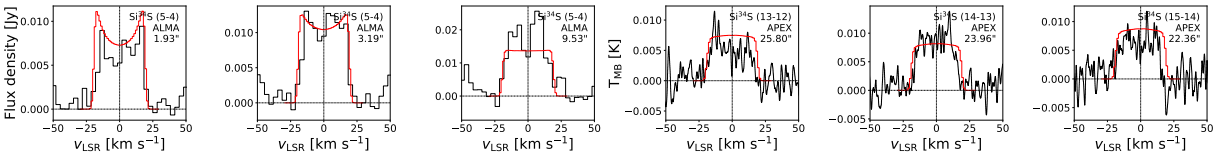

Fig. B.18: As in Fig. B.1, but for IRAS 15082-4808, Si^{34}S

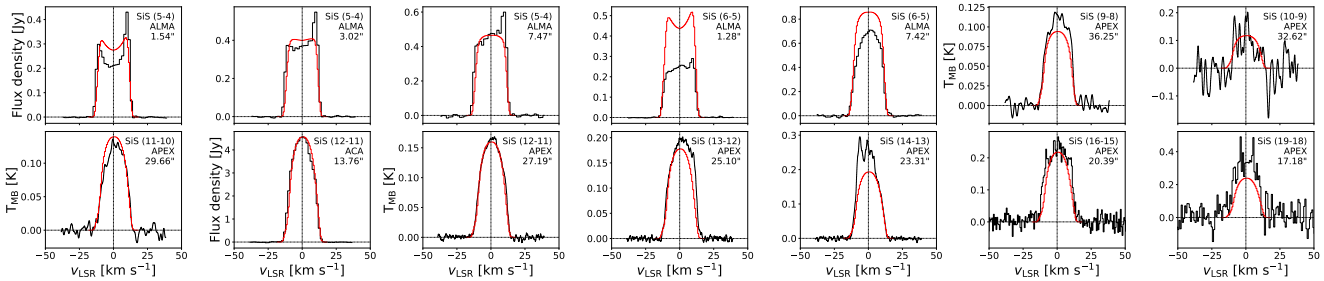

Fig. B.19: As in Fig. B.1, but for IRAS 07454-7112, SiS

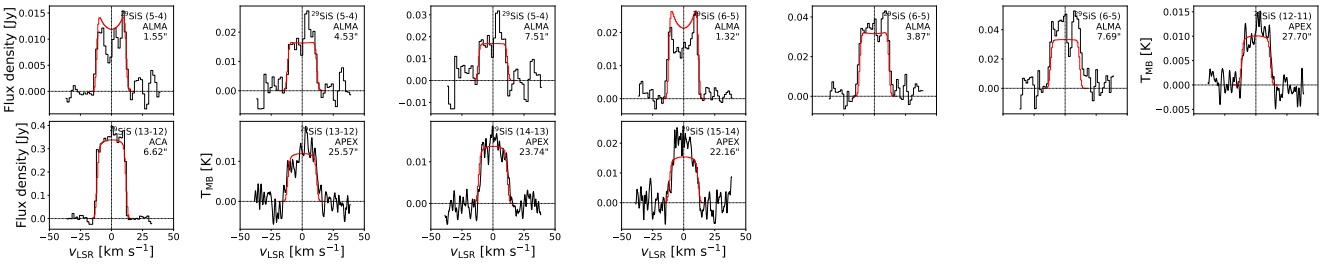

Fig. B.20: As in Fig. B.1, but for IRAS 07454-7112, ^{29}SiS

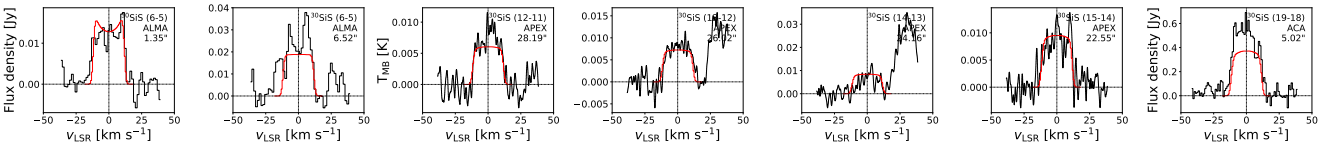

Fig. B.21: As in Fig. B.1, but for IRAS 07454-7112, ^{30}SiS

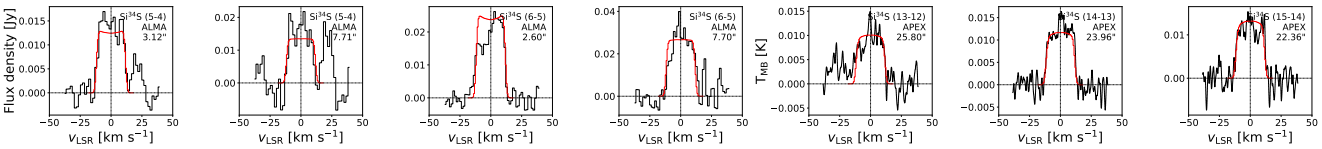

Fig. B.22: As in Fig. B.1, but for IRAS 07454-7112, Si^{34}S

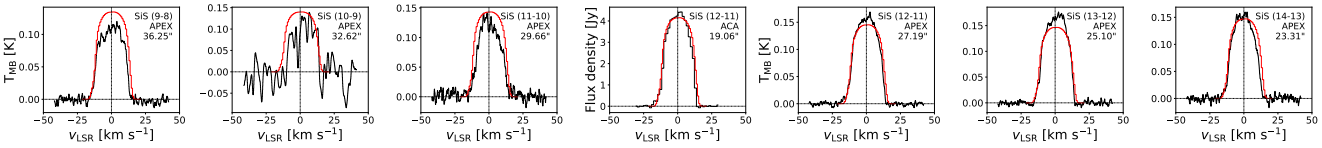

Fig. B.23: As in Fig. B.1, but for AFGL 3068, SiS

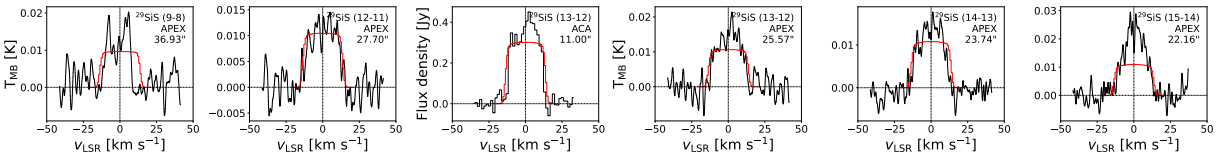

Fig. B.24: As in Fig. B.1, but for AFGL 3068, ^{29}SiS

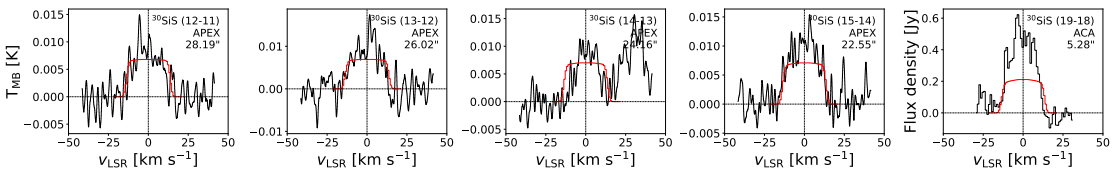

Fig. B.25: As in Fig. B.1, but for AFGL 3068, ^{30}SiS

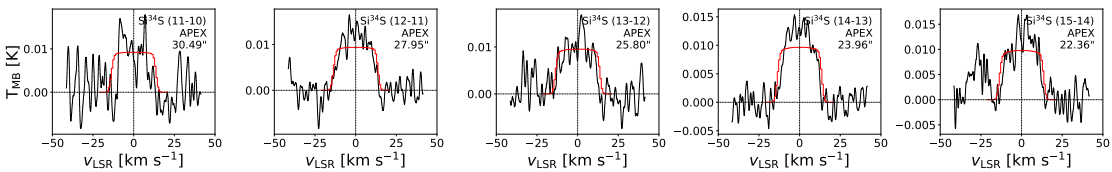

Fig. B.26: As in Fig. B.1, but for AFGL 3068, Si^{34}S

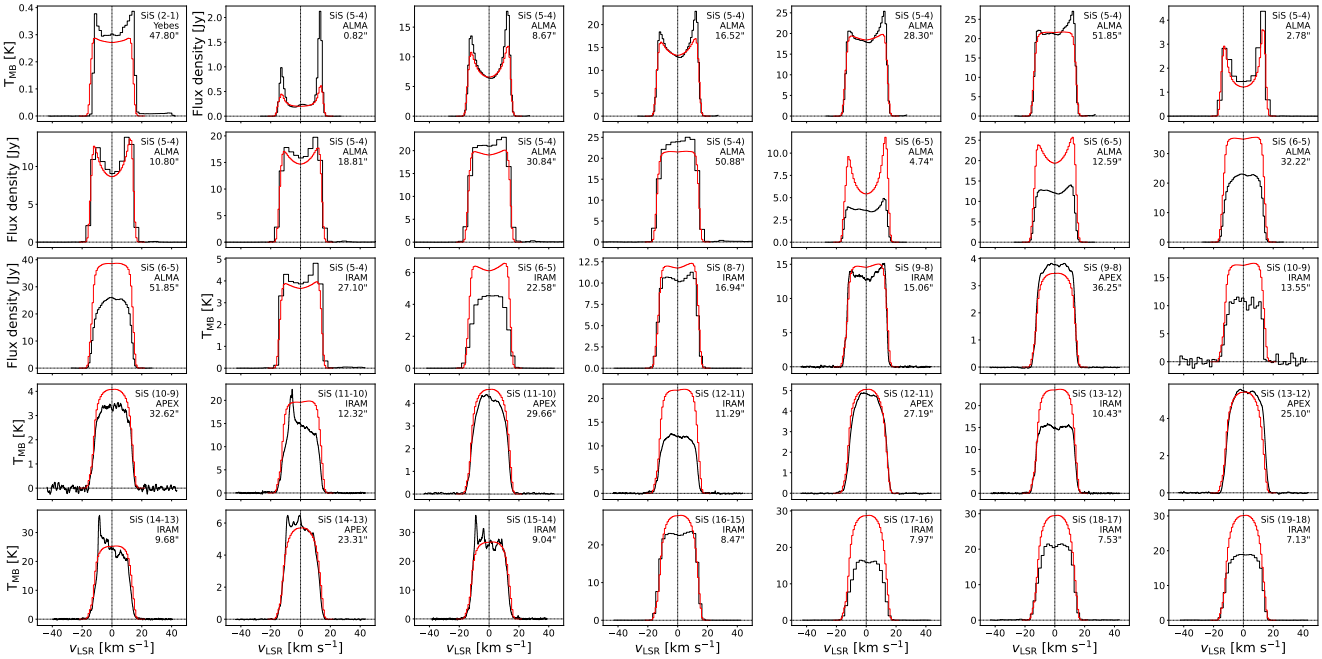

Fig. B.27: As in Fig. B.1, but for IRC+10216, SiS

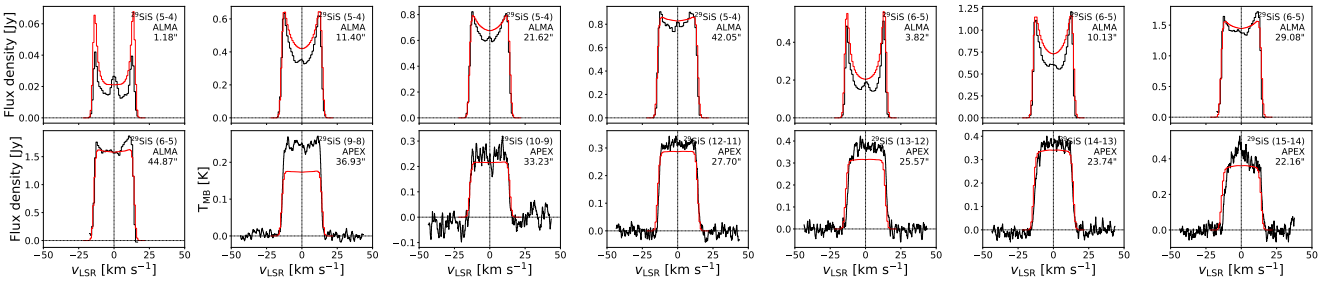

Fig. B.28: As in Fig. B.1, but for IRC+10216, ^{29}SiS

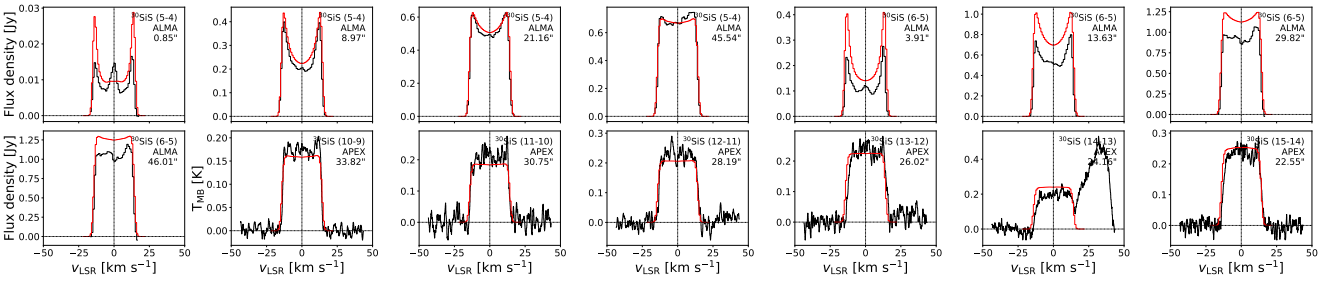

Fig. B.29: As in Fig. B.1, but for IRC+10216, ^{30}SiS

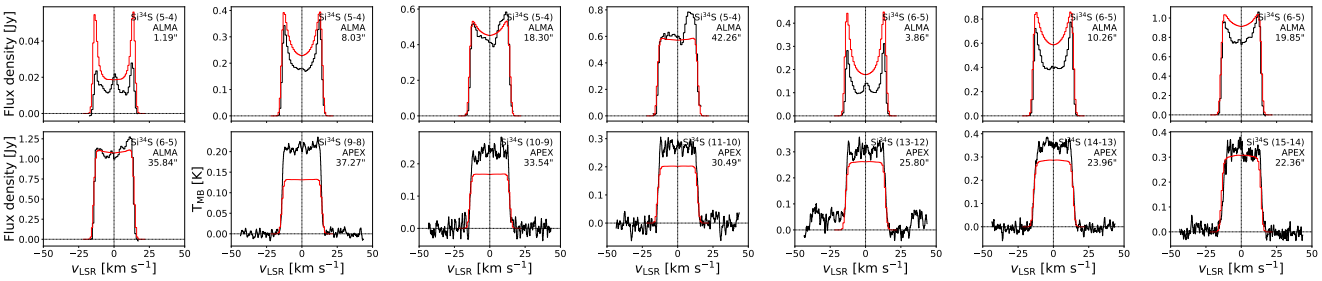

Fig. B.30: As in Fig. B.1, but for IRC+10216, Si^{34}S